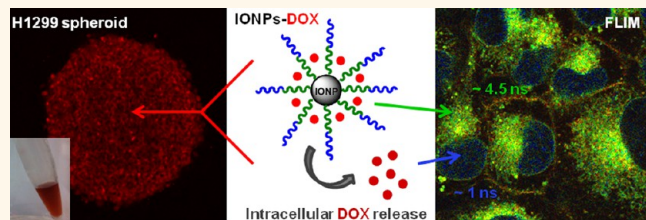


# Using Fluorescence Lifetime Imaging Microscopy to Monitor Theranostic Nanoparticle Uptake and Intracellular Doxorubicin Release

Johan S. Basuki,<sup>†</sup> Hien T.T. Duong,<sup>†</sup> Alexander Macmillan,<sup>§</sup> Rafael B. Erlich,<sup>†,‡</sup> Lars Esser,<sup>†,§</sup> Mia C. Akerfeldt,<sup>‡</sup> Renee Megan Whan,<sup>§</sup> Maria Kavallaris,<sup>†,‡</sup> Cyrille Boyer,<sup>†,\*</sup> and Thomas P. Davis<sup>†,\*</sup>

<sup>†</sup>Australian Centre for Nanomedicine, University of New South Wales, Sydney, New South Wales 2052, Australia, <sup>‡</sup>Children Cancer Institute Australia, Lowy Cancer Research Centre, University of New South Wales, PO Box 81, Randwick, Sydney, New South Wales 2031, Australia, <sup>§</sup>Biomedical Imaging Facility, University of New South Wales, Sydney, New South Wales, 2052 Australia, and <sup>†</sup>Monash Institute of Pharmaceutical Sciences, Monash University, Parkville, Melbourne, Victoria 3052, Australia

**ABSTRACT** We describe the synthesis of iron oxide nanoparticles (IONPs) with excellent colloidal stability in both water and serum, imparted by carefully designed grafted polymer shells. The polymer shells were built with attached aldehyde functionality to enable the reversible attachment of doxorubicin (DOX) via imine bonds, providing a controlled release mechanism for DOX in acidic environments. The IONPs were shown to be readily taken up by cell lines (MCF-7 breast cancer cells and H1299 lung cancer cells), and intracellular release of DOX was proven using *in vitro* fluorescence lifetime imaging microscopy (FLIM) measurements. Using the fluorescence lifetime difference exhibited by native DOX ( $\sim 1$  ns) compared to conjugated DOX ( $\sim 4.6$  ns), the intracellular release of conjugated DOX was *in situ* monitored in H1299 and was estimated using phasor plot representation, showing a clear increase of native DOX with time. The results obtained from FLIM were corroborated using confocal microscopy, clearly showing DOX accumulation in the nuclei. The IONPs were also assessed as MRI negative contrast agents. We observed a significant change in the transverse relaxivity properties of the IONPs, going from 220 to  $390 \text{ mM}^{-1} \text{ s}^{-1}$ , in the presence or absence of conjugated DOX. This dependence of MRI signal on IONP-DOX/water interactions may be exploited in future theranostic applications. The *in vitro* studies were then extended to monitor cell uptake of the DOX loaded IONPs (IONP@P(HBA)-*b*-P(OEGA) + DOX) into two 3D multicellular tumor spheroids (MCS) grown from two independent cell lines (MCF-7 and H1299) using multiphoton excitation microscopy.



**KEYWORDS:** fluorescence lifetime imaging microscopy (FLIM) · theranostics · iron oxide nanoparticles · phasor plot · living radical polymerization

Theranostics is the collective term used for a newly emerging field of nanotechnology where a single nanoparticle is designed to carry functionalities to instigate both diagnosis and therapy.<sup>1–3</sup> It is now well established that nanoparticles (NP) can be designed to encapsulate/transport a wide variety of chemotherapeutic agents for delivery to cancerous (or diseased) cells.<sup>4–6</sup> Nanoparticles can be designed to target tumors by either targeted or passive processes.<sup>7</sup> Passive targeting is reliant on the size of nanoparticles being smaller than the fenestrations of endothelial cells enabling penetration of the interstitium to allow accumulation in the tumor. The combination of leaky vasculature and

poor lymphatic drainage results in the well-known enhanced permeability and retention (EPR) effect.<sup>8</sup>

The use of nanoparticles as contrast agents for biomedical *in vivo* imaging is also widely reported in the medical/scientific literature with many potential advantages over small molecule contrast agents.<sup>9–12</sup> Magnetic iron oxide nanoparticles have been studied widely for applications in magnetic resonance imaging (MRI),<sup>13–16</sup> stem cell tracking,<sup>14,17</sup> biomolecular separation (*i.e.*, proteins and DNA),<sup>14,18</sup> hyperthermia<sup>14</sup> and drug/gene delivery.<sup>6,9,14,19</sup> Specifically, iron oxide nanoparticles (IONPs) have been applied clinically as MRI contrast agents for the detection of liver lesions and

\* Address correspondence to cboyer@unsw.edu.au, thomas.p.davis@monash.edu.

Received for review August 22, 2013 and accepted October 13, 2013.

Published online October 16, 2013  
10.1021/nn404407g

© 2013 American Chemical Society

adenocarcinoma.<sup>20</sup> In comparison to other noninvasive imaging techniques, MRI has several advantages, such as superb spatial resolution, good soft tissue contrast and zero radiation exposure. In a number of recent studies, IONP contrast agents have been employed as theranostics to deliver therapeutic molecules, including chemotherapy drugs and short interfering ribonucleic acid (siRNA).<sup>21–26</sup> Potentially, IONPs can be used to track therapeutic molecule delivery and monitor localized response allowing physicians to adjust dosing regimens to achieve optimal physiological response. The conjugation of therapeutic molecules to IONPs can be achieved by exploiting polymer layers attached to the nanoparticle surface. Two different strategies can be employed for attaching therapeutic molecules to IONPs; simple, noncovalent, encapsulation of therapeutic molecules into the polymers, using hydrophobic or electrostatic interactions,<sup>27–33</sup> *e.g.*, the delivery of siRNA or doxorubicin (DOX) as reported by Nasongkla *et al.*,<sup>34</sup> Liu *et al.*,<sup>35</sup> and others.<sup>27–31,33,36–39</sup> Alternatively, the covalent attachment of therapeutics *via* a reversible linker can provide an improved control over release and pharmacokinetics. Many linkers are known, with redox-, photo-, pH-, enzymatic, or temperature responsiveness to permit reversible conjugation of therapeutics to scaffolds.<sup>40–46</sup> There are only a limited number of studies describing the conjugation of chemotherapy drugs to hybrid organic/inorganic nanoparticles. Gao and co-workers<sup>43</sup> conjugated DOX directly to IONPs *via* an imine linker, showing an enhanced release of DOX at pH 5.4 and relative stability at pH 7.4. However, in this highly promising approach the drug loading was limited by the grafting density of the aldehyde groups on the IONPs surface, and intracellular drug delivery was inferred (rather than proven) using fluorescence uptake data, which is unable to distinguish between conjugated or free DOX.

In this present work, we build on the previous work of Gao and co-workers,<sup>43</sup> with a synthetic approach allowing more versatility in DOX loading. We have synthesized IONPs stabilized with functional polymers with a capability to attach DOX *via* a pH-responsive imine bond. Phosphonic acid terminated poly(4-O-acryloyl benzaldehyde-*b*-oligoethylene glycol-acrylate) block copolymers were made by reversible addition–fragmentation transfer (RAFT) polymerization. The copolymers were grafted “onto” IONPs *via* a simple sonication technique using the strong affinity of the phosphonic end group to anchor onto the IONP surface. The poly(oligoethylene glycol acrylate) block provides a hydrophilic, antifouling and biocompatible layer to the IONPs,<sup>47,48</sup> and the poly(4-O-acryloyl benzaldehyde) provides functional groups suitable for DOX conjugation *via* Schiff base/imine bond. The imine bond is pH-labile, breaking in acidic media (pH typically  $\sim$ 5.5) suitable for potential release in a tumor

environment.<sup>49,50</sup> We then employed two powerful microscopy techniques, multiphoton and confocal microscopy, as well as fluorescence lifetime imaging microscopy (FLIM) to monitor IONP uptake using both 2D and 3D cell models. Using FLIM in 2D cell monolayers, we were able to identify and distinguish both conjugated and native (free) DOX in live cells. To our best knowledge, this report is the first to demonstrate the potential use of FLIM and phasor plot representation to monitor the *in situ* release of DOX from nanoparticles *via* the intracellular degradation of pH-responsive bonds (imine). The 3D multicellular spheroid model provided an insight into the penetration depth of IONP@P(HBA)-*b*-P(OEGA) + DOX to spheroids, in comparison with native DOX. In addition, released DOX was tracked in different compartments of the cells using FLIM and confocal microscopy. We also assessed the magnetic properties of the IONPs as potential contrast agents in MRI and ascertained the potential for signaling on drug release. Finally, we studied the cytotoxicity of the drug conjugated nanoparticles using *in vitro* lung (H1299) and breast (MCF-7) cancer cell lines.

## RESULTS AND DISCUSSION

### Synthesis and Characterization of Doxorubicin Functionalized

**Magnetic Nanoparticles.** Well-defined IONPs with a typical size of 10 nm were coated with phosphonic acid terminated poly(4-O-acryloyl benzaldehyde-*b*-oligoethylene glycol-acrylate) block copolymers (P(HBA)-*b*-P(OEGA)) prepared by grafting “onto” using the strong affinity of the phosphonic acid group for IONP surfaces. First, phosphonic acid terminated P(HBA)-*b*-P(OEGA) copolymer was made by reversible addition–fragmentation transfer polymerization (RAFT) by sequential chain extension in the presence of HBA and OEGA monomers using a new phosphonic acid RAFT agent (Scheme S1 in the Supporting Information). The polymerization proceeded in a controlled fashion as indicated by a linear molecular weight increase *versus* monomer conversion (Figure S1 in the Supporting Information) and a low final polydispersity (PDI  $<$  1.4) (Figure 1A). The composition of P(HBA)-*b*-P(OEGA) copolymer was chosen to contain 30 and 50 units of HBA and OEGA, respectively, as confirmed by <sup>1</sup>H NMR spectroscopy (Figure 1B). The P(HBA) block introduced aldehyde functionality for further attachment of doxorubicin (DOX), while P(OEGA) conferred hydrophilicity and antifouling properties.

Figure 2 showed the grafting strategy used to graft P(HBA)-*b*-P(OEGA) copolymer onto IONPs, with a typical size of 10 nm, as determined by XRD and BET measurements (Figure S2 in the Supporting Information), to yield IONPs@P(HBA)-*b*-P(OEGA) with a hydrodynamic size around 60 nm. The presence of copolymers on the IONP surface was confirmed using a range of

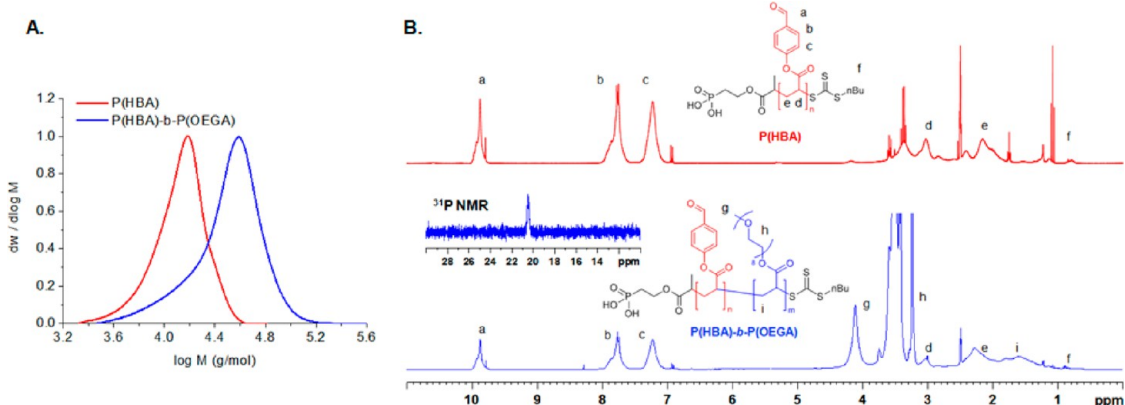


Figure 1. (A) SEC and (B) NMR ( $^1\text{H}$  and  $^{31}\text{P}$ ) spectra of P(HBA) and P(HBA)-b-P(OEGA) copolymers.

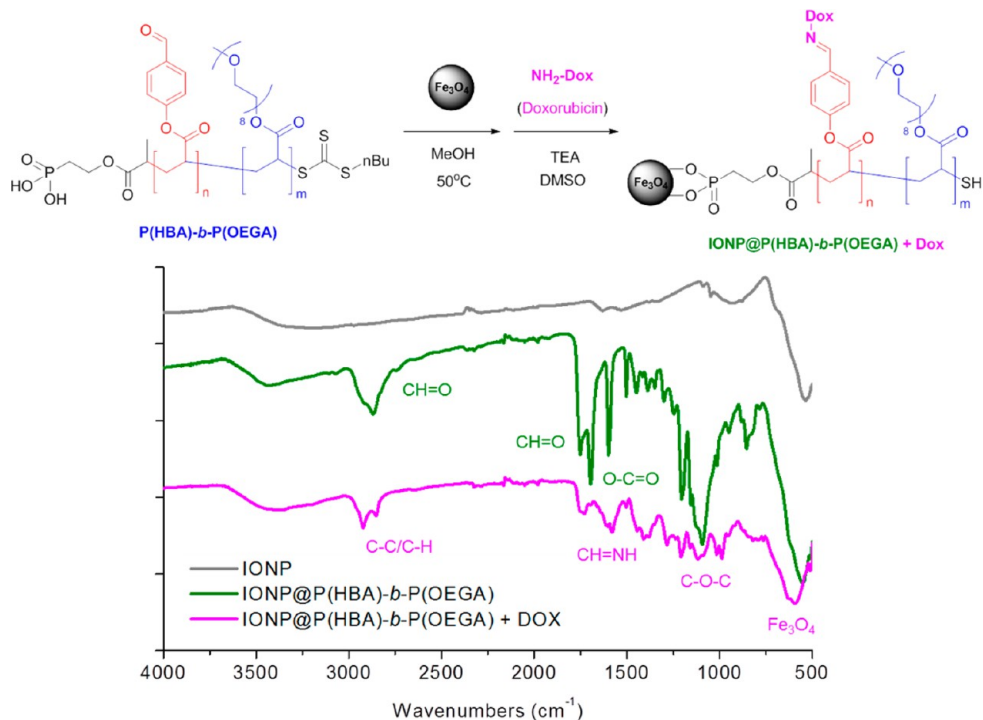


Figure 2. (top) Schematic representation of functionalization of IONP with P(HBA)-b-P(OEGA) followed by conjugation of doxorubicin via Schiff base (Imine); (bottom) ATR-FTIR spectra of naked IONP, IONP@P(HBA)-b-P(OEGA) with and without doxorubicin.

techniques, including XPS, ATR-FTIR and thermal gravimetric analysis (TGA).

The aldehyde group was exploited for the attachment of doxorubicin (DOX) under slightly basic conditions (triethylamine) (Figure 2). The solution was incubated overnight to allow for the attachment of DOX to the polymer layers *via* a pH responsive bond (Schiff base/imine). The IONP solution was then purified by dialysis against water to remove any excess DOX. Finally, IONP@P(HBA)-b-P(OEGA) + DOX was isolated as a dispersion in water and characterized using several techniques, including TGA, UV-visible, ATR-FTIR, fluorescence spectroscopy and XPS spectroscopy.

ATR-FTIR spectra (Figure 2) of IONP@P(HBA)-b-P(OEGA) confirmed the presence of ester, aldehyde

and ether bonds at 1730, 1710, and 1150  $\text{cm}^{-1}$ , respectively. After conjugation with doxorubicin, we noted the absence of signals from the aldehyde bond at 1710  $\text{cm}^{-1}$ . A new absorption was observed at  $\sim 1620 \text{ cm}^{-1}$  consistent with the formation of a Schiff base group (imine).<sup>44</sup>

X-ray photoelectron spectroscopy (XPS) was invoked to further characterize the nanoparticles before and after doxorubicin conjugation (Figure 3). In comparison to nonfunctionalized IONPs, the XPS spectra of polymer functionalized IONP@P(HBA)-b-P(OEGA) displayed a significant increase in the carbon signal at 280 eV. An observed decrease in the signals from iron (Fe) at 720 eV was in accord with a highly grafted polymer layer on the surface of the magnetic

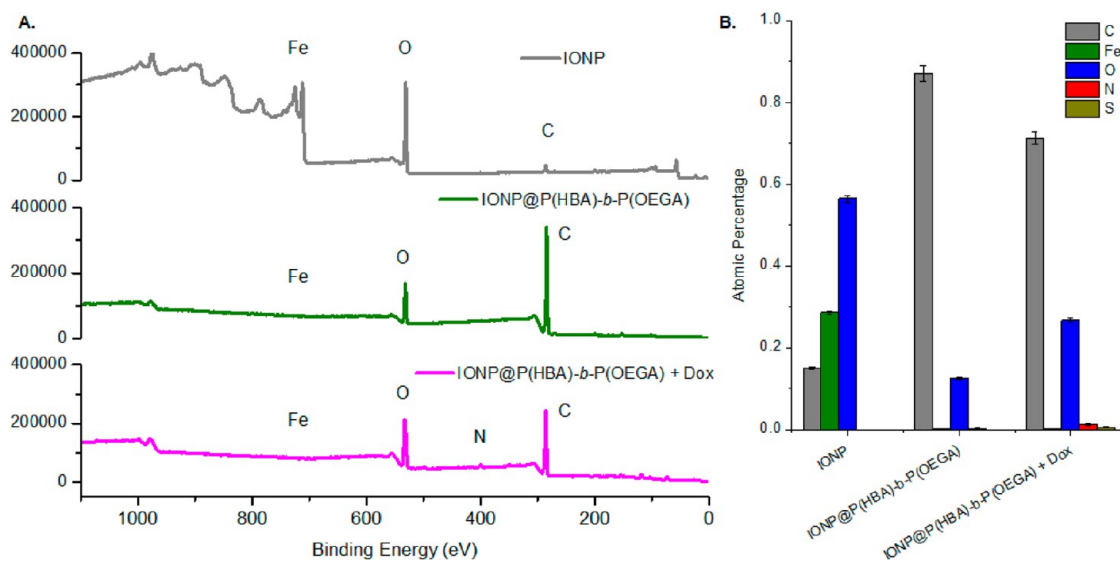


**Figure 3.** XPS Spectra (A) and the atomic percentage (B) of IONP@P(HBA)-b-P(OEGA) with and without doxorubicin. C1s and N1s spectra are included in Figure S4 in the Supporting Information.

nanoparticles. After conjugation with doxorubicin, a nitrogen signal was observed (~2%) at ~399 eV consistent with the presence of doxorubicin on the surface of the nanoparticles, attached *via* Schiff bonds (signal at ~288 eV).<sup>44</sup>

Thermogravimetric analyses (TGA) were used to determine the polymer content in IONP@P(HBA)-b-P(OEGA) and to provide insight into the efficiency of the doxorubicin conjugation reaction (Figure 4). About 42% weight loss was observed on IONP@P(HBA)-b-P(OEGA) consistent with a grafting density of around 0.15 polymer chain per nm<sup>2</sup> (Table 1). After conjugation with doxorubicin, a higher weight loss was observed (~58%), corresponding to a 16 wt. % drug loading. Knowing the approximate number of aldehyde groups per polymer chain (~30 groups/chain), the doxorubicin conjugation efficiency was calculated to be ~67%.

**Colloidal Stability Study of Doxorubicin Functionalized Magnetic Nanoparticles.** Colloidal stability of the functionalized nanoparticles (with and without doxorubicin) was investigated using dynamic light scattering (Table 1) to monitor particle size and aggregation in water. IONP@P(HBA)-b-P(OEGA) has a number average particle size of ~90 nm, with a low dispersity ( $D_{\text{DLS}}^{\text{N}}$  0.15). After conjugation with doxorubicin, the stability of the nanoparticles is slightly improved, as indicated by a decrease in particle size to ~60 nm. IONP@P(HBA)-b-P(OEGA) + DOX did not exhibit any aggregation or precipitation for a period of 6 days in water or serum (see Figure S4 in the Supporting Information). We hypothesize that this excellent colloidal stability is underpinned by the conjugated hydrophobic DOX causing enhanced phase separation in the block copolymer structures, ensuring that the inner block shrinks, compacting the outer P(OEGA) layer, imbuing more resistance to serum protein interactions.

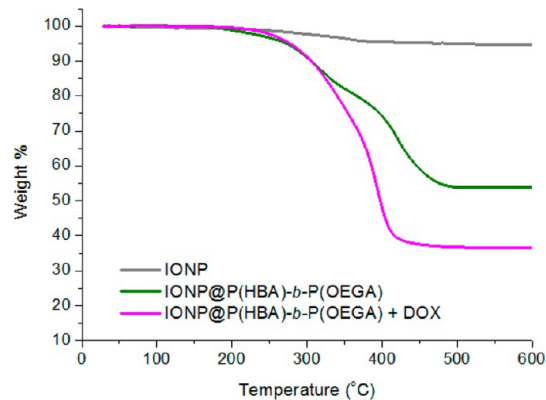


**Figure 4.** Thermogravimetric analyses (TGA) performed on IONP@P(HBA)-b-P(OEGA) with and without conjugated doxorubicin.

The enhanced colloidal stability of doxorubicin functionalized IONPs was also confirmed by scanning electron microscopy (SEM) and transmission electron microscopy (TEM) analyses (Figure 5A and B, respectively) showing different sized structures when compared with similar SEM and TEM measurements on naked IONPs. After conjugation with doxorubicin, IONP@P(HBA)-b-P(OEGA) + DOX gave smaller particle sizes (~60 nm) than IONP@P(HBA)-b-P(OEGA) (~90 nm), which is in good agreement with DLS results (Table 1).

#### pH-Mediated Doxorubicin Release from Functionalized IONPs.

The imine bond has been employed previously for drug conjugation to allow drug release from scaffolds or nanoparticles in acidic media.<sup>44,51,52</sup> In order to compare the drug release profiles at different pH, the doxorubicin functionalized nanoparticles were incubated in both pH 7 phosphate buffer and pH 5 acetate buffer at 37 °C (Figure 6). pH 5 was utilized to mimic the acidic environment in the endosomes and lysosomes.<sup>53</sup> Samples were taken at different time

**TABLE 1. TGA and DLS Results for IONP@P(HBA)-*b*-P(OEGA) Nanoparticles with and without Conjugated Doxorubicin (Measurement Performed in Triplicate)**

	weight loss by TGA (%)	grafting density by TGA ( $\text{nm}^{-2}$ )	number-weighted particle size by DLS (nm) in water
IONP@P(HBA)- <i>b</i> -P(OEGA)	42 $\pm$ 2	0.152 $\pm$ 0.005	90.6 $\pm$ 9.1
IONP@P(HBA)- <i>b</i> -P(OEGA) + DOX	58 $\pm$ 2	0.152 $\pm$ 0.005	64.3 $\pm$ 14.7

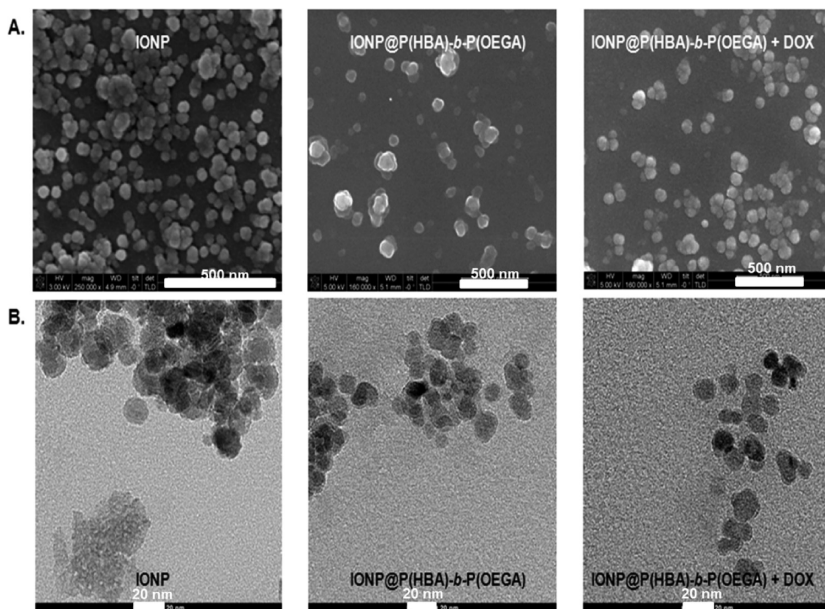


**Figure 5.** SEM (A) and TEM (B) images of naked IONP and IONP@P(HBA)-*b*-P(OEGA) with and without doxorubicin.

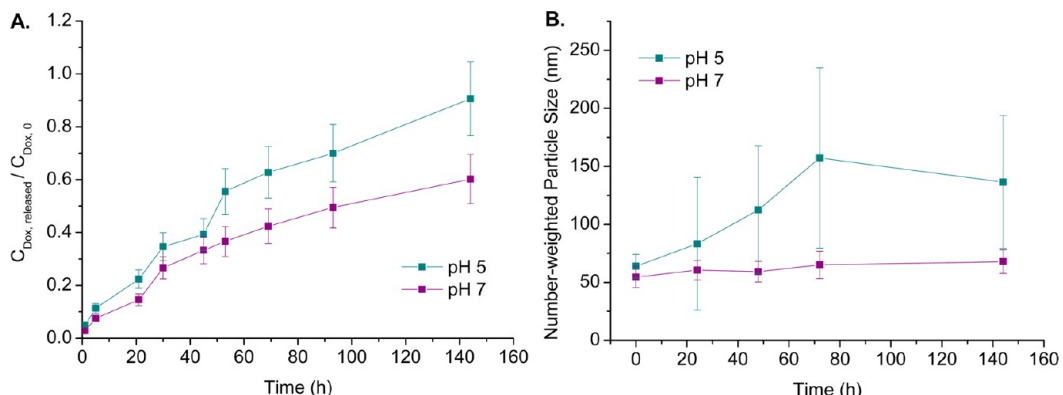


**Figure 6.** (A) Doxorubicin release at pH 5 (acetate buffer) and pH 7 (phosphate buffer) at 37 °C; (B) DLS number size of IONP@P(HBA)-*b*-P(OEGA) + DOX versus time. The measurement was performed in triplicate using two different batches of nanoparticles.

points, and IONPs were separated from the supernatant by centrifugation, followed by analysis using UV-visible and fluorescence spectroscopy to determine the released doxorubicin (*via* a calibration curve). As expected, at pH 5, doxorubicin was released faster than at pH 7, following rapid hydrolysis of the imine bonds in acidic media. About 90% release was achieved at pH 5 after 6 days of incubation, in comparison with only 50% release at pH 7. We observed some nanoparticle aggregation after 6 days of incubation in pH 5 buffer, while in contrast, the nanoparticles in pH 7 buffer remained stable. This increase in colloidal

instability on DOX release is consistent with our earlier observation and hypothesis that conjugated DOX actually increases the colloidal stability of IONPs.

**MRI Contrast Agent Relaxivity Measurements.** IONPs can be employed as negative MRI contrast agents. The magnetic properties of the polymer functionalized iron oxide nanoparticles were investigated (Figure 7).

$T_2$  relaxation times were measured at different iron concentrations in water using a 9.4 T magnetic resonance imaging (MRI) scanner. The  $r_2$  relaxivity of IONP@P(HBA)-*b*-P(OEGA) was found to be significantly higher ( $\sim 386 \text{ mM}^{-1} \text{ s}^{-1}$ ) before doxorubicin

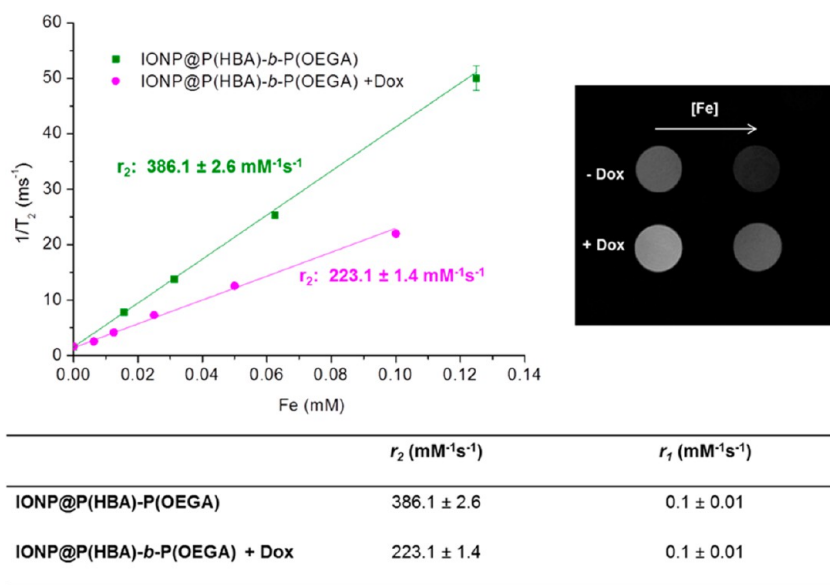


Figure 7. MRI  $T_2$  relaxation study of IONP@P(HBA)-b-P(OEGA) with and without doxorubicin in water at different iron concentrations using a 9.4 T magnetic field.

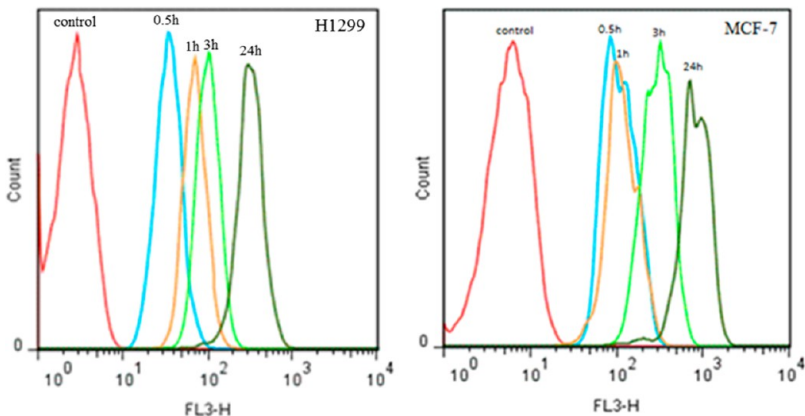
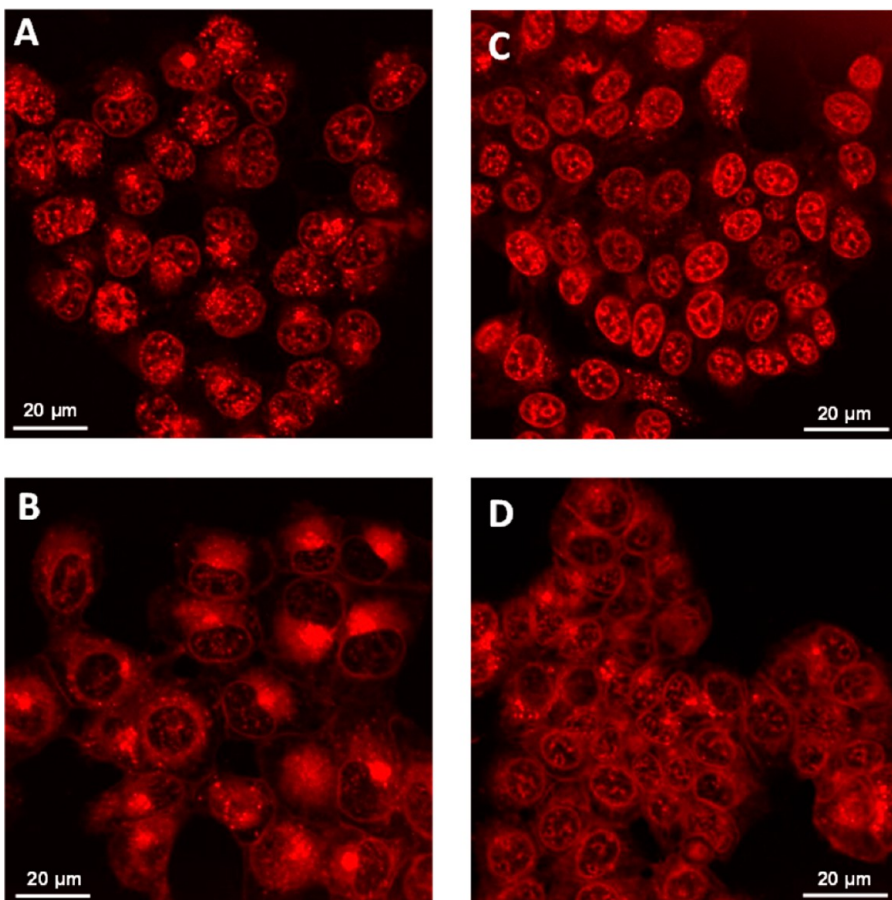


Figure 8. Flow cytometry showing increasing uptake of IONP@P(HBA)-b-P(OEGA) + DOX over a 24 h period using H1299 (left) and MCF-7 (right) cells.

conjugation ( $\sim 223 \text{ mM}^{-1} \text{ s}^{-1}$ ). In  $T_2$ -weighted scans,  $r_2$  high relaxivity and low  $r_1$  relaxivity are desired.<sup>42</sup> Nanoparticles (with and without doxorubicin) yielded a low  $r_1$  relaxivity of  $0.01 \text{ mM}^{-1} \text{ s}^{-1}$ , ideal for negative contrast imaging. Although the  $r_2$  relaxivities of both nanoparticles were found to be high, the absence of doxorubicin enhanced the measured relaxivity by 40%, which was associated with less stable IONP@P(HBA)-b-P(OEGA). Lower  $r_2$  relaxivity of IONP@P(HBA)-b-P(OEGA) + DOX was consistent with our earlier observations on colloidal stability, where an enhanced hydrophobic inner polymer layer altered the access of water to the iron core, attributed to the occupancy of doxorubicin in the inner polymeric layer. Previously, a change in transverse relaxivity was also described for IONPs coated with different polymers. In these early works, the authors attributed the variation of relaxivity ( $r_2$ ) with water accessibility.<sup>22,46,54,55</sup> This significant difference in  $r_2$  relaxivity observed for the magnetic

nanoparticles with and without conjugated doxorubicin could potentially be used in theranostic applications to monitor DOX release *in situ*, and is visually exemplified in the MRI contrast images shown in Figure 7.

**In Vitro Cell Accumulation by Flow Cytometry, Confocal Laser Scanning Microscopic Microscopy, and FLIM Analysis for Monolayer Cells.** IONP@P(HBA)-b-P(OEGA) + DOX were tested *in vitro* with two different cancer cell-lines: lung (H1299) and breast cancer (MCF-7). The fluorescent properties of DOX can be exploited for uptake studies using flow cytometry and fluorescence microscopy *in vitro*. DOX accumulation in both lung cancer cells (H1299) and breast cancer cells (MCF-7) was examined over time *via* flow cytometry. The data shown in Figure 8 demonstrates a rapid accumulation of DOX in the cells after 30 min incubation with the IONP@P(HBA)-b-P(OEGA) + DOX nanoparticles as indicated by an increase in fluorescence intensity, *versus* the nontreated cells by



**Figure 9.** CLSM showing cellular accumulation and distribution of (A) native DOX and (B) IONP@P(HBA)-*b*-P(OEGA) + DOX in H1299 cells; (C) native DOX and (D) IONP@P(HBA)-*b*-P(OEGA) + DOX using MCF-7 cells; after 5 h of incubation. Higher magnifications are shown in Figure S7 in the Supporting Information).

flow cytometry. DOX accumulation continued to increase over a 24 h period as indicated by an increase in fluorescence intensity over time. (For comparison with free DOX, see Figures S5 and S6 in the Supporting Information).

Confocal laser scanning microscopy (CLSM) was also used to confirm the accumulation of native (free) DOX and IONP@P(HBA)-*b*-P(OEGA) + DOX by taking advantage of the intrinsic fluorescent emission of DOX between 565 and 630 nm (Figure 9). Both H1299 and MCF-7 cell lines exhibited the accumulation of native (free) DOX in the nuclei, while in contrast, IONP@P(HBA)-*b*-P(OEGA) + DOX treated cells showed accumulation in both the cytoplasm and the nuclei (when compared to control cells after 5 h of incubation). It is important that DOX accumulates in the cell nuclei, as one of the described mechanisms of DOX depends on its intercalation with DNA with subsequent inhibition of macromolecular biosynthesis.<sup>56</sup> The complementarity of the two methods, quantitative flow cytometry and qualitative fluorescence, proved to be a useful tool for the study of the cellular uptake of DOX and IONP@P(HBA)-*b*-P(OEGA) + DOX in the H1299 and MCF-7 cells.

Unequivocal proof of intracellular DOX release from the nanoparticles cannot be gleaned from conventional intensity based techniques (flow cytometry and CLSM) alone. It is not possible to distinguish between free and conjugated DOX as both forms have similar excitation and emission profiles (Figure S8 in the Supporting Information). To probe intracellular release, we invoked fluorescence lifetime imaging microscopy (FLIM), as in recent work by our group and others, FLIM has proved to be a powerful tool to monitor dynamic DOX release from polymeric nanoparticles.<sup>44,57–60</sup> The fluorescence lifetime of a fluorophore corresponds to the average time a molecule stays in its excited state before returning to ground state. In general, the fluorescence lifetime is critically dependent upon the physicochemical environment that surrounds the probe.<sup>61</sup> FLIM provides an intensity independent measurement, and in the context of this work, FLIM can be used to monitor the changes in DOX fluorescence lifetimes on the basis of its microenvironment: (i) native (free) DOX in media, (ii) DOX conjugated to IONPs in media, (iii) native DOX released from pH-responsive IONPs in the cellular organelles, and (iv) DOX conjugated to IONPs in the

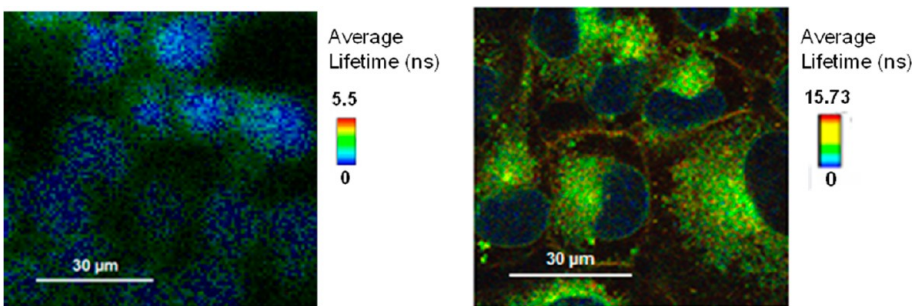


**Figure 10.** FLIM images showing cell uptake of native DOX (left) and IONP@P(HBA)-b-P(OEGA) + DOX (right) using H1299 cells after 5 h of incubation (false color range 0–5.5 ns). Blue color corresponds to the short lifetime ( $\sim 1.6$  ns), while green color corresponds to the longer lifetime ( $\sim 4.6$  ns) (no membrane dye was employed). The cell membrane appears as the IONP@P(HBA)-b-P(OEGA) + DOX are absorbed on the cell surfaces. The FLIM image denotes the fluorescence lifetimes measured at each pixel and displayed as color contrast image. The corresponding false-color lookup table represents the lifetime distribution.

cellular organelles. FLIM is a noninvasive and concentration independent technique that can monitor the spatial variations of fluorescence lifetime within single live cells.

The fluorescence lifetimes straight after the addition of native (free) DOX and IONP@P(HBA)-b-P(OEGA) + DOX in media solution containing H1299 and MCF-7 cells were first measured using time-correlated single photon counting (TCSPC). The concentration-independent single exponential decay corresponding to a lifetime of 1.0 ns for native (free) DOX is consistent with known published lifetime values,<sup>57</sup> and an average lifetime of 4.6 ns was determined for DOX encapsulated within IONPs. An increase in DOX lifetime has been previously observed for DOX encapsulated in polymeric nanoparticles.<sup>44,57,58</sup> The fluorescence lifetimes of native (free) DOX and DOX + IONP@P(HBA)-b-P(OEGA) are substantially different, enabling differentiation in solution, making FLIM ideal for monitoring *in vitro* DOX release from IONPs.

FLIM was performed using native DOX in lung H1299 and breast MCF-7 cancer live cells (at a concentration of  $0.5 \mu\text{M}$  based on DOX) for 1, 5, and 24 h of incubation. The lifetime of DOX increased to 1.6 ns in the nucleus from its corresponding value in media solution (1.0 ns). The increased lifetime of DOX in the nucleus can be attributed to the well-accepted DOX–DNA intercalation, inducing cellular apoptotic cell death.<sup>62</sup> Figure 10 shows the fluorescence lifetime distribution of native DOX in H1299 cells after 5 h of incubation. The bimodal lifetime distribution was observed in both cell lines H1299 when treated with IONP@P(HBA)-b-P(OEGA) + DOX. The fluorescence lifetime distribution of DOX shows differences consistent with DOX partitioned between the nucleus and the cytoplasm. The average fluorescence lifetimes are 1.6 ns in the nucleus (attributed to DOX released from IONPs) and 4.6 ns in the cytoplasm (attributed to the conjugated DOX to IONP@P(HBA)-b-P(OEGA) in the cytoplasm after endocytosis). Similar results were obtained using MCF-7 cells (data not shown). The release

of DOX from IONP@P(HBA)-b-P(OEGA) + DOX can therefore be traced by interpreting the change in lifetime values depending on the accumulation of DOX in different cell compartments. FLIM allows us to reliably distinguish and detect both native DOX and IONP@P(HBA)-b-P(OEGA) + DOX in the same voxel (otherwise hampered by the overlapping fluorescence emission spectra).

In this study, we additionally used phasor plot analysis to map the data recorded using FLIM (Figure S9 in the Supporting Information). Phasor analysis presents the fluorescence lifetime data in a graphical form, negating the need for exponential fitting to the fluorescence decay.<sup>63–65</sup> Phasor plotting was originally developed to overcome some of the drawbacks of FLIM, such as the low photon counts per pixel, which renders differentiation between one and two lifetimes difficult.<sup>65</sup> In phasor analysis of lifetime images, lifetime data at each pixel is transformed into a phasor plot. All single exponential lifetimes lie on the universal circle, while multiexponential lifetimes are a linear combination of their components (Figure S9 in the Supporting Information). The first successful use of phasor plot analysis to study DOX release from dextran nanoparticles was recently reported by our group.<sup>44</sup> In the present work, DOX was covalently attached via pH-responsive bonds onto IONP polymer shells. As demonstrated in Figure 6, DOX release from IONP@P(HBA)-b-P(OEGA) + DOX can be easily monitored in model reactions using buffer solutions, indicating the effect of pH on mediating the breakage of the imine bonds. However, while indicative, the model reactions provide no guarantee of effective intracellular bond breakage and DOX release. This motivated us to determine the fluorescence lifetime of DOX over periods of time in live cells.

As seen in Figure 11, the longer fluorescence lifetime contribution to the phasor plot (highlighted in red) is predominant after 1 h of DOX-IONP incubation in H1299 cells. Over 24 h of incubation, there is a time dependent shift to shorter fluorescence lifetimes

(highlighted in green (5 h) and orange (24 h)) in Figure 11. This phasor plot shift indicates that there is an increase in the fractional contribution to fluorescence from released DOX over time. FLIM images for H1299 cells demonstrate an increasing concentration of released DOX with shorter fluorescence lifetime in the nucleus (Figure S10 in the Supporting Information).

**3D Observation of DOX and IONP@P(HBA)-b-P(OEGA) + DOX Penetration Analysis to Cellular Spheroids.** Preclinical research relies heavily on two-dimensional (2D) monolayer cell culture; however, there is an increasing interest in three-dimensional (3D) models.<sup>66–68</sup> 3D cell culture is superior to 2D cell culture in representing the 3D network of the cell–cell and cell–environment interactions in tumors.<sup>69,70</sup> Multicellular tumor spher-

oids (MCS) are one of the classic 3D culture models, which is an *in vitro* culture intermediate between monolayer culture and *in vivo* tumor. MCSs offer many advantages over traditional 2D monolayer cell cultures in the investigation of dynamics and pharmacokinetics of chemotherapeutic drugs, as the response of cells in 3D MCS is more correlative with *in vivo* models than cells grown as 2D monolayer. Several studies have demonstrated differences in drug sensitivity between 2D and 3D cultures for chemotherapeutic drugs.<sup>71,72</sup> For example, breast cancer cells grown in 2D cultures differ in cytotoxic response when grown in 3D cultures.<sup>73</sup> In the present study, multicellular tumors spheroid assays based on the lung cancer cell line H1299 and breast cancer cells MCF-7 were evaluated in order to investigate tissue distributions and penetration depth of DOX and IONP@P(HBA)-b-P(OEGA) + DOX. Microscopic study of living tumor spheroids at increasing imaging depth, however, is challenging because of the increased light scattering.<sup>74</sup> To overcome this problem, multiphoton excitation microscopy was used providing 3D optical sectioning without absorption above and below the plane of focus.<sup>75</sup> As a result of the longer excitation wavelength, multiphoton excitation microscopy offers increased depth penetration into living tissue (when compared to conventional confocal microscopy).<sup>75</sup> After incubation for 17 h, with native (free) DOX or IONP@P(HBA)-b-P(OEGA) + DOX (concentration of 5  $\mu$ M based on DOX), individual spheroids from MCF-7 and H1299 3D cultured samples were imaged every 5  $\mu$ m section from the top to bottom. The 3D images of the spheroids were reconstructed using Imaris software (Figure 12 and

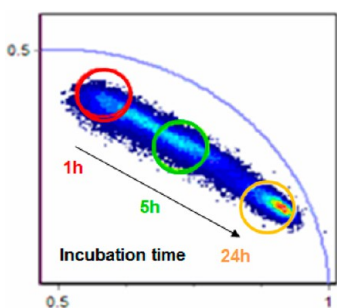


**Figure 11.** Phasor plot derived from the FLIM images for H1299 lung cancer cells at different incubation times (1, 5, and 24 h) with IONP@P(HBA)-b-P(OEGA) + DOX. Red ROI (region of interest) corresponds to the signal after 1 h of incubation; green ROI and orange ROI correspond to the signals after 5 and 24 h, respectively. Each ROI corresponds to different lifetimes of DOX in the cells corresponding to different amounts of DOX released from IONP@P(HBA)-b-P(OEGA) + DOX.

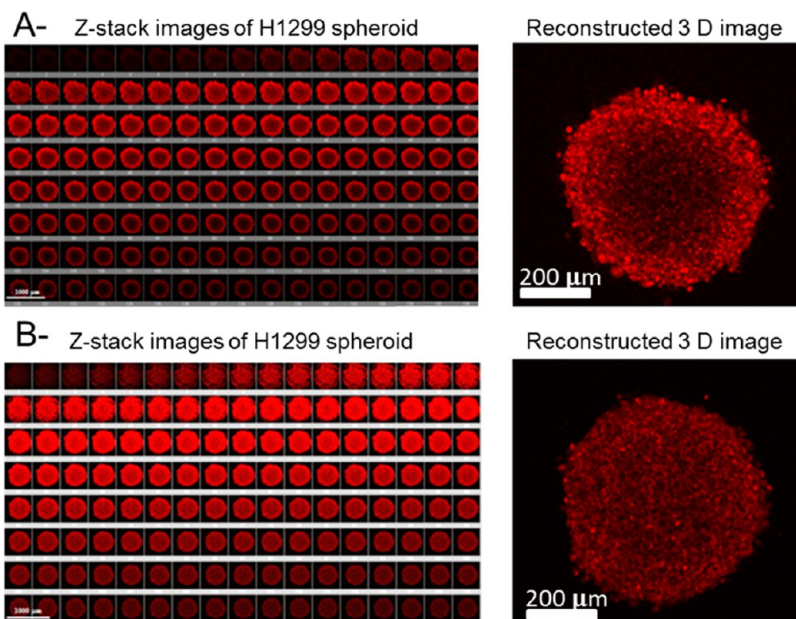


**Figure 12.** 3D images of H1299 spheroids after incubation (A) with native (free) DOX and (B) with IONP@P(HBA)-b-P(OEGA) + DOX for 17 h (concentration of 5  $\mu$ M based on DOX). The representative confocal images (left) were taken every 5  $\mu$ m section from the top to bottom in the middle of an intact spheroid, whereas the 3D image (right) was reconstructed using Imaris software.

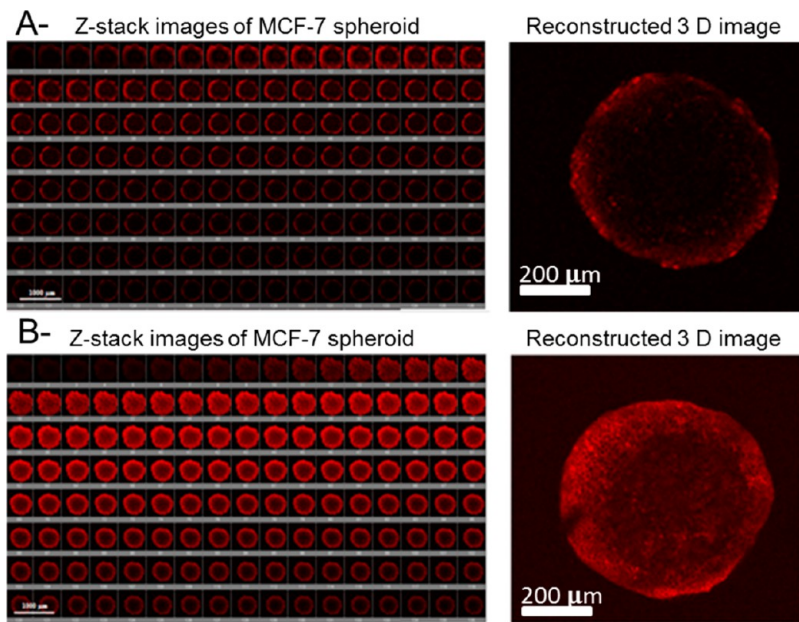


Figure 13. 3D images of MCF-7 spheroids after incubation with (A) native (free) DOX and (B) IONP@P(HBA)-*b*-P(OEGA) + DOX for 17 h (concentration of 5  $\mu$ M based on DOX). The representative confocal images (left) were taken every 5  $\mu$ m section from the top to bottom in the middle of an intact spheroid, whereas the 3D image (right) was reconstructed using Imaris software.

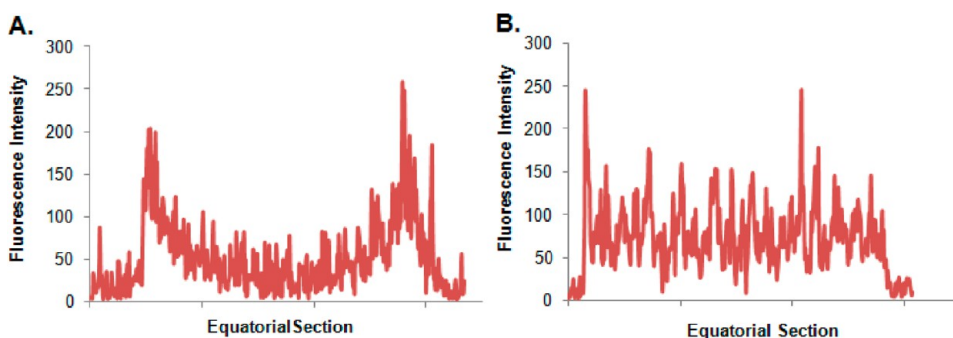


Figure 14. Fluorescence intensity distribution along a horizontal line across the optical section of the equatorial plane of H1299 spheroids after incubation with (A) free DOX and (B) IONP@P(HBA)-*b*-P(OEGA) + DOX for 17 h (concentration of 5  $\mu$ M based on DOX).

Figure 13). Interestingly, IONP@P(HBA)-*b*-P(OEGA) + DOX clearly penetrated deeper in the 3D spheroid when compared to native DOX for both cancer cell lines (after 17 h incubation).

Figure 14 (data not shown for MCF-7) shows the equatorial sections of H1299 MCS loaded with DOX and IONP@P(HBA)-*b*-P(OEGA) + DOX incubated for 17 h. The fluorescence intensity decreased from the rim of the equatorial section to the center, indicating limited penetration of native DOX. The fluorescence distribution along the horizontal line across the equatorial section shows that the fluorescence intensity of the central part is negligible when compared to that of the periphery. The fluorescence distribution histogram shows DOX accumulation in the peripheral rim of thickness 40  $\mu$ m. However, it is noteworthy that IONP@P(HBA)-*b*-P(OEGA) + DOX can fully penetrate into the MCS for both cell lines after incubation with

5  $\mu$ M DOX equivalent for 17 h as indicated by the homogeneous DOX staining of tissue. This discrepancy of penetration can be attributed to the different transport pathways of free DOX and IONP@P(HBA)-*b*-P(OEGA) + DOX. The internalization of IONPs into the spheroids could be influenced by transferrin, a molecule involved in iron transport. The penetration mechanism, however, is still unclear and is ongoing research in our group.

The toxicities of IONP@P(HBA)-*b*-P(OEGA) and IONP@P(HBA)-*b*-P(OEGA) + DOX and native DOX were assessed against the lung cancer cell line H1299, breast cancer cell line MCF-7, and normal lung fibroblasts MRC5 (Figures S11, S12, and S13 in the Supporting Information). First, IONPs and IONP@P(HBA)-*b*-P(OEGA) were nontoxic at all concentrations examined in this study after 72 h (data not shown); thus, any future influence on cell viability from DOX loaded

**TABLE 2. Comparison of  $IC_{50}$  ( $\mu$ M) Values for Doxorubicin and Doxorubicin Loaded IONPs in MRC5 Normal Fibroblast Cells, MCF-7 Breast Cancer Cells, and H1299 Lung Cancer Cells,  $n = 3$**

cell line	$IC_{50}$ ( $\mu$ M)	$IC_{50}$ ( $\mu$ M)
cell line	free DOX	IONP@P(HBA)-b-P(OEGA) + DOX
MRC-5	0.174 $\pm$ 0.028	0.233 $\pm$ 0.033
MCF-7	0.069 $\pm$ 0.015	0.038 $\pm$ 0.008
H1299	0.121 $\pm$ 0.016	0.079 $\pm$ 0.012

nanoparticles cannot be attributed to the toxicity of polymers or IONPs. It is noted that IONP@P(HBA)-b-P(OEGA) + DOX exhibited certain cytotoxicity for all three tested cell lines. The normal MRC5 cells were less susceptible than the H1299 and MCF-7 cells to both native and conjugated DOX. Therefore,  $IC_{50}$  values of IONP@P(HBA)-b-P(OEGA) + DOX for the MRC5 were  $\sim 3$  fold higher than those for H1299 cells and  $\sim 6$  fold for MCF-7 cells (Table 2). Interestingly, IONP@P(HBA)-b-P(OEGA) + DOX present an enhanced toxicity (lower in  $IC_{50}$ ) than native DOX for both cancerous cell lines providing the potential application of IONPs as an efficient drug delivery vehicle. In summary, our studies have demonstrated that DOX loaded IONPs are taken up and can effectively deliver their drug load to H1299 and MCF-7 cell nuclei (demonstrated by FLIM and CLSM), resulting high cytotoxicities in lung and breast cancer cell lines.

## CONCLUSIONS

In this study, we have demonstrated the functionalization of IONPs using P(HBA)-b-P(OEGA) block copolymers *via* a grafting “onto” approach. Aldehyde groups were exploited to conjugate DOX *via* imine/Schiff base pH-responsive reversible bonds. The IONP@P(HBA)-b-P(OEGA) + DOX nanoparticles exhibited excellent colloidal stability in different media, including fetal calf serum. Flow cytometry and confocal microscopy both confirmed nanoparticle accumulation in lung and breast cancer cell lines. Additionally, nanoparticle accumulation and subsequent, pH dependent intracellular release of DOX was proven using FLIM with phasor plot analysis. Furthermore the FLIM data furnished information on the kinetic of DOX accumulation in the cell nuclei, in accord with confocal microscopy images. Importantly, for future potential theranostic applications, the release of DOX significantly enhanced the proton transverse relaxivity of the IONPs showing proven contrast differences in MRI. The cell uptake in 3D spheroids was also investigated for both cancer cell lines. The nanoparticle-transported DOX, IONP@P(HBA)-b-P(OEGA) + DOX, showed enhanced penetration into the 3D multicellular spheroids when compared to native DOX. Finally, toxicity studies show that DOX loaded into IONPs show enhanced toxicity over native DOX in lung and breast cancer cell lines.

## EXPERIMENTAL SECTION

Materials and methods are described in the Supporting Information

**Synthetic Procedures.** *Synthesis of Magnetite Nanoparticles (IONP).* 40 mL of 2 M  $FeCl_3 \cdot 6H_2O$  (0.08 mol, 21.6 g) in 1 M HCl and 20 mL of 2 M  $FeCl_2 \cdot 4H_2O$  (0.04 mol, 9.3 g) in 1 M HCl were mixed, and the mixture was diluted to 0.6 L with deionized water. 125 mL of  $N_2$  prepurged 28%  $NH_4OH$  solution was then slowly added into the solution of iron chloride, and the mixture was vigorously stirred for 30 min. The formation of a black precipitate of magnetite was immediately observed, and the precipitate was then collected under a magnetic field. The magnetic nanoparticles were extensively washed with deionized water to remove unreacted materials and impurities. An aqueous dispersion of magnetite (about 15 mg/mL of  $Fe_3O_4$ ) was prepared by sonication of the magnetite nanoparticles in water at pH 5.5. The dispersion was sonicated for 15 min at 25 W with a sonicator 3000 Misonix.

*Synthesis of RAFT Agent 1*Step 1. 3.9 mL (2.83 g, 0.028 mol) of triethylamine was added to a 45 mL solution of dimethyl(2-hydroxyethyl) phosphonate in anhydrous dichloromethane (4 g, 0.026 mol). After 15 min of stirring, 2-bromopropionyl bromide (2.9 mL, 0.028 mol) was added slowly to the reaction mixture at 0 °C, and the reaction was stirred at room temperature overnight; then, the white precipitate was filtered off, and the clear filtrate was extracted with (2  $\times$  200 mL) saturated sodium bicarbonate in water, followed by (1  $\times$  200 mL) water. The solution was then dried over anhydrous  $MgSO_4$ . Dimethyl 2-(2-bromopropionyloxy)ethyl phosphonate was obtained as an oil-like product after filtration and solvent evaporation:  $^1H$  NMR (300 MHz) in  $CDCl_3$   $\delta$  1.69 (d, 3H), 2.03–2.14 (dt, 2H), 3.01–3.08 (m, 1H), 3.63 (d, 6H), 4.22–4.27 (dt, 2H);  $^{31}P$  NMR (300 MHz) in  $CDCl_3$   $\delta$  29.1 ppm. Step 2. Initially, 2.85 mL of

*n*-butylthiol (0.026 mol, 2.3 g) was dissolved in 30 mL of dichloromethane. Then 7.1 mL of triethylamine (0.051 mol, 5.2 g) was added slowly at 0 °C, followed by 1.5 mL of carbon disulfide (0.026 mol, 1.95 g). The solution was stirred at room temperature for 2 h to yield an orange precipitate. Without purification, 7.4 g of dimethyl 2-(2-bromopropionyloxy)ethyl phosphonate (0.013 mol) was dissolved in 10 mL of methylene chloride and added subsequently to the solution of *n*-butyl trithiocarbonate salt. The reaction mixture was stirred at room temperature for 20 h. The mixture was washed with water (2  $\times$  200 mL) and extracted with dichloromethane (2  $\times$  200 mL). After drying over anhydrous  $MgSO_4$  the solvent from the organic phase was removed under a vacuum. The residue was subjected to a silica flash chromatography using 1:1 ethyl acetate/*n*-hexane to provide 8.15 g of yellowish oil of product, 2-(*n*-butyltrithiocarbonate)-propionic acid 2-(dimethoxyphosphonyl)-ethyl ester (total yield 85%):  $^1H$  NMR (300 MHz) in  $CDCl_3$   $\delta$  0.88 (t, 3H), 1.36 (m, 2H), 1.53 (d, 3H), 1.63 (m, 2H), 2.08–2.2 (dt, 2H), 3.3 (t, 2H), 3.69 (d, 6H), 4.26–4.35 (dt, 2H);  $^{31}P$  NMR (300 MHz) in  $CDCl_3$   $\delta$  29.2 ppm. Step 3. 2-(*n*-Butyltrithiocarbonate)-propionic acid 2-(dimethoxyphosphonyl)-ethyl ester (3 g, 0.008 mol) was dissolved in 23 mL of anhydrous methylene chloride. Subsequently, 4.2 mL (0.04 mol, 6.1 g) of bromotrimethylsilane was added dropwise, and the mixture was stirred at room temperature for 3 h. The solvent and volatile residues were removed then by evaporation, and the silylated intermediate was cleaved by adding a large excess of methanol (24 mL). The mixture was stirred at room temperature for another 2 h, followed by solvent evaporation to provide yellowish oil. The crude RAFT agent was dissolved in diethyl ether (50 mL) and was washed with water (2  $\times$  20 mL). After drying over anhydrous  $MgSO_4$ , the solvent from the organic phase was removed under a vacuum. This crude RAFT agent **1** was purified through a silica flash column chromatography

using ethyl acetate, which resulted in 0.9 g of product, 2-(*n*-butyltrithiocarbonate)-propionic acid 2-ethyl phosphonic acid, in a form of a yellow oil (total yield 33%):  $^1\text{H}$  NMR (300 MHz) in DMSO- $d_6$   $\delta$  0.88 (t, 3H,  $\text{SCH}_2\text{CH}_2\text{CH}_2\text{CH}_3$ ), 1.36 (m, 2H,  $\text{SCH}_2\text{CH}_2\text{CH}_2\text{CH}_3$ ), 1.53 (d, 3H,  $\text{SCH}(\text{CH}_3)\text{COO}$ ), 1.63 (m, 2H,  $\text{SCH}_2\text{CH}_2\text{CH}_2\text{CH}_3$ ), 1.9–1.94 (m, 2H,  $\text{P}(\text{OH})_2\text{CH}_2\text{CH}_2\text{O}$ ), 3.38 (t, 2H,  $\text{SCH}_2\text{CH}_2\text{CH}_2\text{CH}_3$ ), 4.22 (t, 2H,  $\text{P}(\text{OH})_2\text{CH}_2\text{CH}_2\text{O}$ ), 4.68–4.75 (m,  $\text{SCH}(\text{CH}_3)\text{COO}$ );  $^{13}\text{C}$  NMR (300 MHz) in  $\text{CDCl}_3$   $\delta$  171.8 ( $\text{SCH}(\text{CH}_3)\text{COO}$ ), 59.4 ( $\text{P}(\text{OH})_2\text{CH}_2\text{CH}_2\text{O}$ ), 52.9 ( $\text{SCH}(\text{CH}_3)\text{COO}$ ), 47.8 ( $\text{SCH}_2\text{CH}_2\text{CH}_2\text{CH}_3$ ), 37.1 ( $\text{P}(\text{OH})_2\text{CH}_2\text{CH}_2\text{O}$ ), 29.9 ( $\text{SCH}_2\text{CH}_2\text{CH}_2\text{CH}_3$ ), 22 ( $\text{SCH}_2\text{CH}_2\text{CH}_2\text{CH}_3$ ), 17 ( $\text{SCH}(\text{CH}_3)\text{COO}$ ), 13.6 ( $\text{SCH}_2\text{CH}_2\text{CH}_2\text{CH}_3$ );  $^{31}\text{P}$  NMR (300 MHz) in DMSO- $d_6$  (proton decoupled)  $\delta$  20.1 ppm; HRMS (ESI)  $m/z$  calculated for  $\text{C}_{10}\text{H}_{19}\text{O}_5\text{PS}_3 + \text{Na}^+$  [M + Na] $^+$  369.000, found 369.023.

**Synthesis of Monomer HBA (4-O-Acryloyl benzaldehyde).** 12.5 mL (9.1 g, 0.09 mol) of triethylamine was added to a 120 mL solution of anhydrous dichloromethane containing 10 g (0.082 mol) of 4-hydroxy benzaldehyde. After 15 min of stirring, 7.8 g (0.086 mol) of acryloyl chloride was added slowly to the reaction mixture at 0 °C, and the reaction was held at room temperature overnight; then, the white precipitate was filtered off, and the clear filtrate was extracted with (2  $\times$  200 mL) saturated sodium bicarbonate in water, followed by (1  $\times$  200 mL) water. The solution was then dried over anhydrous  $\text{MgSO}_4$ . 4-O-acryloyl benzaldehyde was obtained as white solid product after solvent evaporation (yield 86%):  $^1\text{H}$  NMR (300 MHz) in  $\text{CDCl}_3$   $\delta$  6.03 (d, 1H,  $\text{CH}_2=\text{CHCOO}$ ), 6.30 (dd, 1H,  $\text{CH}_2=\text{CHCOO}$ ), 6.60 (d, 1H,  $\text{CH}_2=\text{CHCOO}$ ), 7.28 (d, 2H,  $\text{OC}_6\text{H}_4\text{CHO}$ ), 7.8 (d, 2H,  $\text{OC}_6\text{H}_4\text{CHO}$ ), 9.95 (s, 1H,  $\text{OC}_6\text{H}_4\text{CHO}$ );  $^{13}\text{C}$  NMR (300 MHz) in  $\text{CDCl}_3$   $\delta$  122.3 ( $\text{OC}_6\text{H}_4\text{CHO}$ ), 127.4 ( $\text{CH}_2=\text{CHCOO}$ ), 131.2 and 133.5 ( $\text{OC}_6\text{H}_4\text{CHO}$ ), 134 ( $\text{CH}_2=\text{CHCOO}$ ), 155.3 ( $\text{OC}_6\text{H}_4\text{CHO}$ ), 163.8 ( $\text{CH}_2=\text{CHCOO}$ ), 190.9 ( $\text{OC}_6\text{H}_4\text{CHO}$ ).

**Synthesis of P(HBA).** RAFT agent **1** (24.6 mg, 0.071 mmol), AIBN (2.3 mg, 0.014 mmol) and 4-O-acryloyl benzaldehyde or HBA (0.5 g, 2.84 mmol) were dissolved in dioxane (5 mL) in septa sealed vials. The vials were placed in an ice bath, and the solutions were purged with nitrogen for 30 min. The ratio between the monomer, RAFT agent **1** and AIBN in the polymerization medium  $[\text{Monomer}]_0$ : $[\text{RAFT}]_0$ : $[\text{Initiator}]_0$  was 40:1:0.1. After deoxygenation, the reaction mixture was then placed in an oil bath at 70 °C. After 8 h of reaction, the reaction was quenched *via* rapid cooling and exposure to oxygen. The reaction was directly analyzed by  $^1\text{H}$  NMR and DMAc GPC to determine the monomer conversion and the molecular weight. The polymer was concentrated by partial evaporation of solvent, and the polymer was precipitated in 1:1 diethyl ether/*n*-hexane three times to remove the nonreacted monomer and RAFT agent. The purified polymer was then dried under a vacuum overnight to give 0.38 g of a yellow-white solid. On the basis of HBA conversion of 75%, the yield of the polymer was calculated as 99%. The purified product was further characterized by  $^1\text{H}$  NMR,  $^{31}\text{P}$  NMR, and DMAc GPC.

**Synthesis of P(HBA)-*b*-P(OEGA).** The P(HBA), previously obtained, was used as a macroRAFT agent (0.2 g,  $M_n \sim 5000$  g/mol (based on  $^1\text{H}$  NMR), *i.e.*, 0.04 mmol of polymer) in the presence of oligoethylene glycol acrylate or OEGA monomers (1.15 g,  $M_n \sim 480$  g/mol, 2.4 mmol). AIBN (1 mg, 0.006 mmol) as initiator was added to the solution of 2.5 mL of anhydrous acetonitrile, which was then purged with nitrogen for 30 min. The ratio between the monomer, macroRAFT agent P(HBA), and the initiator in the polymerization medium  $[\text{Monomer}]_0$ : $[\text{macroRAFT}]_0$ : $[\text{Initiator}]_0$  was 60:1:0.15. Polymer chain extension was carried out at 60 °C overnight (20 h). At the end of polymerization, the polymers were precipitated in a cold 1:1 mixture of diethyl ether and *n*-hexane (3 times) and then, dialyzed using MWCO = 12 000 Da, in acetone. On the basis of OEGA conversion of 83%, the yield of the polymer was calculated as 86%. The purified polymer was then dried under a vacuum overnight to give 1 g of a yellowish gel-like solid. The resultant block copolymer was characterized by DMAc GPC, FTIR,  $^1\text{H}$  NMR, and  $^{31}\text{P}$  NMR.

**Nanoparticle Functionalization Procedures. Grafting of P(HBA)-*b*-P(OEGA) onto Magnetite Nanoparticles: IONP@P(HBA)-*b*-P(OEGA).** Iron oxide nanoparticles IONP (10 mg), were dispersed in water (1 mL). 0.2 g of P(4HBA)-*b*-P(OEGA), ( $M_n$ , DMAc GPC = 27 300 g/mol, PDI = 1.38) was dissolved in methanol (4 mL).

An aqueous dispersion of iron oxide nanoparticles was diluted with methanol (5 mL), and the solution of block copolymer was added slowly to the IONP dispersion. The resulting dispersion was sonicated for 15 min (power = 25 W), followed by incubation in a shaker overnight at 50 °C. The mixture was filtered to remove any unstabilized particles and centrifuged (using an Eppendorf Centrifuge 5804) for 30 min (14 000 rpm/min). The functionalized iron oxide nanoparticles were isolated at the base of the centrifuge tube. The supernatant was removed, and the particles were redispersed in methanol using sonication for 10 min. This washing process was repeated twice. The resultant functionalized iron oxide nanoparticles IONP@P(HBA)-*b*-P(OEGA) were dried and subsequently redispersed in DMSO (around 4 mg/mL of functionalized IONP) by using the sonicator for 20 min ( $P$  = 20 W). Material characterization was carried out using TGA, XPS, TEM, and DLS.

**Conjugation of Doxorubicin with IONP@P(HBA)-*b*-P(OEGA).** 1.5 mg (0.00276 mmol) of doxorubicin HCl (9 mg as doxorubicin HCl in lactose matrix) was dissolved in 1 mL of DMSO. 3.75  $\mu\text{L}$  of triethylamine (0.0267 mmol) was added to the solution of doxorubicin. The solution was stirred for 15 min and then added to 0.5 mL of IONP@P(HBA)-*b*-P(OEGA). The mixture was incubated at room temperature overnight and then dialyzed using cellulose membrane with MWCO 12 000 Da in water. After dialysis, the dispersion of doxorubicin functionalized magnetic nanoparticles IONP@P(HBA)-*b*-P(OEGA) + DOX was stored in the refrigerator. The nanoparticles were characterized by TGA, UV-vis, fluorescence spectroscopy, DLS, and XPS.

**Doxorubicin Release Study in pH 5 and 7 Buffer from IONP@P(HBA)-*b*-P(OEGA) + DOX.** 0.25 mL of the IONP@P(HBA)-*b*-P(OEGA) + DOX was added to 10 mL of pH 5 acetate buffer (simulating the pH conditions of endosomes and lysosomes) and pH 7 phosphate buffer solution. The mixture was shaken in the incubator at 37 °C up to 6 days. At defined time points, samples (1 mL) were taken and centrifuged through a membrane (MWCO 3000 Da). The supernatant was collected in the centrifugal membrane tube and analyzed by fluorescence spectroscopy to determine the concentration of released doxorubicin (excitation 470 nm). The volume was kept constant during the experiments. The experiments were carried out in triplicate. The results are presented as an average (standard deviation was calculated using origin).

**Biological Assay of IONP@P(HBA)-*b*-P(OEGA) + DOX (DOX-IONPs). Cell Culture Assays.** The human lung cancer cells H1299, human breast cancer cells MCF-7, and normal fetal lung fibroblasts MRC5 were grown in Dulbecco's Modified Eagle's Medium: Nutrient Mix F-12 (DMEM) supplemented with 10% (v/v) Fetal Calf Serum (FCS) in a ventilated tissue culture flask T-75. The cells were incubated at 37 °C in a 5%  $\text{CO}_2$  humidified atmosphere and passaged every 2–3 days when monolayers at around 80% confluence were formed. Cell density was determined by counting the number of viable cells using a trypan blue dye (Sigma-Aldrich) exclusion test. For passaging and plating, cells were detached using 0.05% trypsin-EDTA (Invitrogen), stained using trypan blue dye, and loaded on the hemocytometer.

**Cell Viability Assays.** The cytotoxicity of native DOX and IONP@P(HBA)-*b*-P(OEGA) + DOX was tested *in vitro* by a standard Alamar Blue Assay. The assay is based on the ability of living cells to convert blue redox dye (resazurin) into bright red resorufin, which can be read in a spectrophotometric reader. Nonviable cells rapidly lose metabolic capacity and thus do not generate a color signal. Thus, the intensity of the color is proportional to the cell viability. The cells were seeded at 2000 cells/well for H1299 and MCF-7 and 5000 cells/well for MRC5 in 96 well tissue culture plates and incubated for 24 h. The different seeded cell numbers of MRC5 and MCF-7 was dictated by their relative proliferation rates, giving optimal cell densities. We followed the method described in the literature.<sup>76</sup> The medium was then replaced with fresh medium containing native DOX and IONP@P(HBA)-*b*-P(OEGA) + DOX over an equivalent DOX concentration range of 0.001–10  $\mu\text{M}$ . At 72 h post-drug/nanoparticles incubation, treatments were removed, and fresh media was added (100  $\mu\text{L}$ ), followed by the addition of Alamar Blue dye (20  $\mu\text{L}$ ) to each well. The cells were then incubated for 6 h. Cell viability was determined as a percentage

of untreated control cells, and  $IC_{50}$  values were determined by nonlinear regression analyses using Graphpad Prism 6 software.

**In Vitro Cell Accumulation by Flow Cytometry and Confocal Laser Scanning Microscopic Analysis of Monolayer Cells.** IONP@P(HBA)-b-P(OEGA) + DOX cell uptake was measured by flow cytometry; H1299 and MCF-7 cells were seeded at a density of  $1 \times 10^5$  cells/well in 6-well tissue culture plates. The cells were left to grow for 24 h in DMEM media containing 10% FBS at 37 °C in 5% CO<sub>2</sub> atmosphere. After 24 h, IONP@P(HBA)-b-P(OEGA) + DOX were added to the wells (concentration of 0.125  $\mu$ M based on DOX) and the cells were incubated for 30 min, 1 h, 3 h, and 24 h. Following particle incubation, cells were rinsed twice with PBS to remove residual extracellular nanoparticles. Cells were harvested by trypsinization and resuspended in 500  $\mu$ L of PBS for flow cytometry analysis using the FACS Calibur flow cytometer (BD Biosciences). Data shown are the mean fluorescent signal for 10 000 cells. Cells that were not treated with nanoparticle solutions were used as a control. Data was analyzed using the Flowjo software.

Confocal laser scanning microscopy (CLSM) was also used to study the accumulation of native DOX and IONP@P(HBA)-b-P(OEGA) + DOX dynamics in 2D monolayer cultures of living H1299 and MCF-7 cells. For this purpose, H1299 and MCF-7 cells (5000 cells/dish) were plated in 35 mm cultured dishes, which were precoated with poly-D-lysine hydrobromide for 10 min and left to grow for 3 days. CLSM images of cells were obtained using confocal microscopy (Leica TCS SP5 II) with a 60  $\times$  1.4NA oil immersion objective. The microscope stage was enclosed in an environmental chamber allowing for control of temperature, humidity, and atmospheric conditions for live-cell microscopy. The 488-nm line from an argon ion laser was used for excitation, and emission was collected between 565 and 630 nm.

**Fluorescence Lifetime Imaging Microscopy (FLIM).** For FLIM analysis, H1299 and MCF-7 cells were seeded into sterilized 3 cm glass bottom dishes (Mat-Tek) (100 000 cells/well). After 48 h seeding, the medium was replaced with fresh medium containing either native DOX or IONP@P(HBA)-b-P(OEGA) + DOX (0.5  $\mu$ M equivalent DOX concentration), and cells were incubated at 37 °C for 3, 5, and 24 h. Lifetime images were recorded using 60  $\times$ , 1.2 NA water-immersion objective (Olympus).

Fluorescence lifetime imaging (FLIM) was performed on a Picoquant Microtime200 inverted confocal microscope. Excitation was via a fiber-coupled, pulsed laser diode operating at 470 nm (40 MHz) with a pulse width below 200 ps. The emission was collected using a 550 nm long-pass filter and a single-photon avalanche diode (SPAD) (PDM, MicroPhoton Devices) connected to time-correlated single-photon counting (TCSPC) electronics (Picoharp300, Picoquant). Fluorescein was used to calibrate the phasor plot to a monoexponential lifetime of 4 ns.

The data was acquired and analyzed using Symphotime software (Picoquant). Phasor analysis of FLIM data was performed using SimFCS software developed at the Laboratory for Fluorescence Dynamics, University of California at Irvine.

**Generation of Multicellular Tumor Spheroids.** Lung cancer cell line H1299 and breast cancer cell line MCF-7 cellular spheroids were generated using the liquid overlay method.<sup>77</sup> Briefly, cells were grown in Dulbecco's Modified Eagle's Medium: Nutrient Mix F-12 (DMEM) supplemented with 10% (v/v) Fetal Calf Serum (FCS) in a ventilated tissue culture flask T-75. The cells were incubated at 37 °C in a 5% CO<sub>2</sub> humidified atmosphere. When the cells reached approximately 80% confluence, they were harvested by trypsinization and resuspended in DMEM supplemented with 10% (v/v) FCS. Single-cell suspension was seeded to flat-bottom standard 96-well plates. The flat-bottom standard 96-well plates were previously coated with 60  $\mu$ L of a sterile 1.5% (wt/vol) solution of agarose in DMEM to generate a nonadherent surface. To generate multicellular spheroids, 5000 cells suspended in 100  $\mu$ L of culture media were added into each agarose-coated well, and the plates were left for 72 h in a 37 °C humidified incubator with 5% CO<sub>2</sub> until spheroids formed. For subsequent drug treatments and imaging procedures, spheroids were carefully transferred from 96-well plates to fluorodish cell culture dishes. Spheroids with an average diameter of  $\sim$ 400  $\mu$ m after 3 days growth were used for nanoparticle penetration experiments.

**$T_1$  and  $T_2$  Relaxivity Measurement of IONP@P(HBA)-b-P(OEGA).** A 9.4 T Bruker Biospin 94/20 USR equipped with a Transceiver RES <sup>1</sup>H 72 mm Quad RF coil was used for  $T_1$  and  $T_2$  relaxometry measurements. A dilution series for each sample (500  $\mu$ L) was prepared in water or fetal calf serum, and measurements were performed at 20 °C.  $T_2$ -weighted images were acquired using a multi-slice-multi-echo (MSME) sequence with TR = 4000 ms and 32 echoes with echo spacing 10.686 ms, FOV = 5  $\times$  5 cm, matrix size = 256  $\times$  256, scan time = 12 min, and slice thickness 1 mm. A rapid acquisition rapid echo with variable repetition time (RARE-VTR) sequence was used to acquire  $T_1$ -weighted images, with TR = 88, 470, 922, 1474, 2183, 3176, 4869, and 15 000 ms, TE = 8.074 ms, FOV = 5  $\times$  5 cm, matrix size = 128  $\times$  128, RARE factor 2, scan time = 24 min and slice thickness 1 mm. The net magnetizations for each sample were determined from the manually drawn regions of interest (ROIs). The  $T_1$  relaxation times were determined by fitting a monoexponential association equation and the  $T_2$  relaxation times by fitting a monoexponential decay equation using Paravision 5 (Bruker). The  $T_1$  and  $T_2$  relaxivity was then calculated as slope from a plot of the inverse of the relaxation times ( $R_i$ ,  $i = 1, 2$ ) versus iron concentration in water. The iron concentrations were determined by Inductively Coupled Plasma–Optical Emission Spectroscopy (ICP-OES) using a Perkin-Elmer Optima 7300 ICP-OES spectrometer. The nanoparticles were digested overnight in highly concentrated hydrochloric acid (32%), followed by dilution in water.

**DOX Penetration Analysis of Cellular Spheroids Using Multiphoton Microscopy.** Multiphoton microscopy was employed to visualize the penetration of native DOX and IONP@P(HBA)-b-P(OEGA) + DOX into multicellular spheroids. After being exposed to native DOX and IONP@P(HBA)-b-P(OEGA) + DOX (5  $\mu$ M equivalent DOX concentration) for 17 h, H1299 and MCF-7 multicellular spheroids on the third day to trace the penetration of DOX. Images of the spheroids were collected using a Leica TCS SP5 II, MP FCS inverted microscope, equipped with tunable Mai Tai Deep See multiphoton laser (Spectra-Physics, 80 MHz, 120 fs pulse) and a 20  $\times$  water immersion objective. The doxorubicin was excited using a laser with a wavelength at 488 nm, and the resulting emission was collected in NDDs.

**Conflict of Interest:** The authors declare no competing financial interest.

**Acknowledgment:** The authors thank the Nuclear Magnetic Resonance facility, Biomedical Imaging facility and the Electron Microscope Unit at the Mark Wainwright Analytical Centre for helpful discussions and advice on the design of the experimental setup. C.B. is thankful for his fellowship from Australian Research Council (APD-ARC (DP10925640) and Future Fellowship (ARC-FT 120100096)). M.K. is supported by a National Health and Medical Research Council Senior Research Fellowship and a Cancer Council New South Wales Program Grant.

**Supporting Information Available:** Experimental details, analytical instruments, molecular weight distribution, XRD and BET of IONP, FLIM images, cytotoxicity study (Figures S1–S13, Scheme S1). This material is available free of charge via the Internet at <http://pubs.acs.org>.

## REFERENCES AND NOTES

- Koo, H.; Huh, M. S.; Sun, I.-C.; Yuk, S. H.; Choi, K.; Kim, K.; Kwon, I. C. *In Vivo Targeted Delivery of Nanoparticles for Theranosis*. *Acc. Chem. Res.* **2011**, *44*, 1018–1028.
- Caldorera-Moore, M. E.; Liechty, W. B.; Peppas, N. A. Responsive Theranostic Systems: Integration of Diagnostic Imaging Agents and Responsive Controlled Release Drug Delivery Carriers. *Acc. Chem. Res.* **2011**, *44*, 1061–1070.
- Liong, M.; Lu, J.; Kovochich, M.; Xia, T.; Ruehm, S. G.; Nel, A. E.; Tamanoi, F.; Zink, J. I. Multifunctional Inorganic Nanoparticles for Imaging, Targeting, and Drug Delivery. *ACS Nano* **2008**, *2*, 889–896.
- Balazs, A. C.; Emrick, T.; Russell, T. P. Nanoparticle Polymer Composites: Where Two Small Worlds Meet. *Science* **2006**, *314*, 1107–1110.

5. Peer, D.; Karp, J. M.; Hong, S.; Farokhzad, O. C.; Margalit, R.; Langer, R. Nanocarriers as an Emerging Platform for Cancer Therapy. *Nat. Nanotechnol.* **2007**, *2*, 751–760.
6. Huang, H.-C.; Barua, S.; Sharma, G.; Dey, S. K.; Rege, K. Inorganic Nanoparticles for Cancer Imaging and Therapy. *J. Controlled Release* **2011**, *155*, 344–357.
7. Wang, M.; Thanou, M. Targeting Nanoparticles to Cancer. *Pharmacol. Res.* **2010**, *62*, 90–99.
8. Maeda, H. Tumor-Selective Delivery of Macromolecular Drugs via the EPR Effect: Background and Future Prospects. *Bioconjugate Chem.* **2010**, *21*, 797–802.
9. Reddy, L. H.; Arias, J. L.; Nicolas, J.; Couvreur, P. Magnetic Nanoparticles: Design and Characterization, Toxicity and Biocompatibility, Pharmaceutical and Biomedical Applications. *Chem. Rev.* **2012**, *112*, 5818–5878.
10. Krasia-Christoforou, T.; Georgiou, T. K. Polymeric Theranostics: Using Polymer-Based Systems for Simultaneous Imaging and Therapy. *J. Mater. Chem. B* **2013**, *1*, 3002–3025.
11. Terreno, E.; Castelli, D. D.; Viale, A.; Aime, S. Challenges for Molecular Magnetic Resonance Imaging. *Chem. Rev.* **2010**, *110*, 3019–3042.
12. L. Villaraza, A. J.; Bumb, A.; Brechbiel, M. W. Macromolecules, Dendrimers, and Nanomaterials in Magnetic Resonance Imaging: The Interplay between Size, Function, and Pharmacokinetics. *Chem. Rev.* **2010**, *110*, 2921–2959.
13. Boyer, C.; Whitakker, M. R.; Bulmus, V.; Liu, J.; Davis, T. P. The Design and Utility of Polymer Stabilized Iron Oxide Nanoparticles for Nanomedicine Applications. *NPG Asia Mater.* **2010**, *23*–30.
14. Laurent, S.; Bridot, J.-L.; Elst, L. V.; Muller, R. N. Magnetic Iron Oxide Nanoparticles for Biomedical Applications. *Future Med. Chem.* **2010**, *2*, 427–449.
15. Laurent, S.; Forge, D.; Port, M.; Roch, A.; Robic, C.; Vander Elst, L.; Muller, R. N. Magnetic Iron Oxide Nanoparticles: Synthesis, Stabilization, Vectorization, Physicochemical Characterizations, and Biological Applications. *Chem. Rev.* **2008**, *108*, 2064–2110.
16. Arosio, P.; Thevenot, J.; Orlando, T.; Orsini, F.; Corti, M.; Mariani, M.; Bordonali, L.; Innocenti, C.; Sangregorio, C.; Oliveira, H.; et al. Hybrid Iron Oxide-Copolymer Micelles and Vesicles as Contrast Agents for MRI: Impact of the Nanostructure on the Relaxometric Properties. *J. Mater. Chem. B* **2013**, *1*, 5317–5328.
17. Shigdar, S.; Lin, J.; Li, Y.; Yang, C. J.; Wei, M.; Zhu, Y.; Liu, H.; Duan, W. Cancer Stem Cell Targeting: The Next Generation of Cancer Therapy and Molecular Imaging. *Ther. Delivery* **2012**, *3*, 227–244.
18. Okoli, C.; Boutonnet, M.; Mariey, L.; Järås, S.; Rajarao, G. Application of Magnetic Iron Oxide Nanoparticles Prepared from Microemulsions for Protein Purification. *J. Chem. Technol. Biotechnol.* **2011**, *86*, 1386–1393.
19. Gautier, J.; Allard-Vannier, E.; Munnier, E.; Soucé, M.; Chourpa, I. Recent Advances in Theranostic Nanocarriers of Doxorubicin based on Iron Oxide and Gold Nanoparticles. *J. Controlled Release* **2013**, *169*, 48–61.
20. Cole, A. J.; Yang, V. C.; David, A. E. Cancer Theranostics: The Rise of Targeted Magnetic Nanoparticles. *Trends Biotechnol.* **2011**, *29*, 323–332.
21. Jain, T. K.; Morales, M. A.; Sahoo, S. K.; Leslie-Pelecky, D. L.; Labhasetwar, V. Iron Oxide Nanoparticles for Sustained Delivery of Anticancer Agents. *Mol. Pharmaceutics* **2005**, *2*, 194–205.
22. Munnier, E.; Cohen-Jonathan, S.; Linassier, C.; Douziech-Eyrolles, L.; Marchais, H.; Soucé, M.; Hervé, K.; Dubois, P.; Chourpa, I. Novel Method of Doxorubicin-SPION Reversible Association for Magnetic Drug Targeting. *Int. J. Pharm.* **2008**, *363*, 170–176.
23. Yang, L.; Cao, Z.; Sajja, H. K.; Mao, H.; Wang, L.; Geng, H.; Xu, H.; Jiang, T.; Wood, W. C.; Nie, S.; et al. Development of Receptor Targeted Magnetic Iron Oxide Nanoparticles for Efficient Drug Delivery and Tumor Imaging. *J. Biomed. Nanotechnol.* **2008**, *4*, 439–449.
24. Yang, X.; Chen, Y.; Yuan, R.; Chen, G.; Blanco, E.; Gao, J.; Shuai, X. Folate-Encoded and  $\text{Fe}_3\text{O}_4$ -Loaded Polymeric Micelles for Dual Targeting of Cancer Cells. *Polymer* **2008**, *49*, 3477–3485.
25. Yu, M. K.; Jeong, Y. Y.; Park, J.; Park, S.; Kim, J. W.; Min, J. J.; Kim, K.; Jon, S. Drug-Loaded Superparamagnetic Iron Oxide Nanoparticles for Combined Cancer Imaging and Therapy *In Vivo*. *Angew. Chem., Int. Ed.* **2008**, *47*, 5362–5365.
26. Jayakumar, O. D.; Ganguly, R.; Tyagi, A. K.; Chandrasekharan, D. K.; Nair, C. K. K. Water Dispersible  $\text{Fe}_3\text{O}_4$  Nanoparticles Carrying Doxorubicin for Cancer Therapy. *J. Nanosci. Nanotechnol.* **2009**, *9*, 6344–6348.
27. Maeng, J. H.; Lee, D.-H.; Jung, K. H.; Bae, Y.-H.; Park, I.-S.; Jeong, S.; Jeon, Y.-S.; Shim, C.-K.; Kim, W.; Kim, J.; et al. Multifunctional Doxorubicin Loaded Superparamagnetic Iron Oxide Nanoparticles for Chemotherapy and Magnetic Resonance Imaging in Liver Cancer. *Biomaterials* **2010**, *31*, 4995–5006.
28. Nigam, S.; Barick, K. C.; Bahadur, D. Development of Citrate-Stabilized  $\text{Fe}_3\text{O}_4$  Nanoparticles: Conjugation and Release of Doxorubicin for Therapeutic Applications. *J. Magn. Magn. Mater.* **2010**, *323*, 237–243.
29. Kievit, F. M.; Wang, F. Y.; Fang, C.; Mok, H.; Wang, K.; Silber, J. R.; Ellenbogen, R. G.; Zhang, M. Doxorubicin Loaded Iron Oxide Nanoparticles Overcome Multidrug Resistance in Cancer *In Vitro*. *J. Controlled Release* **2011**, *152*, 76–83.
30. Fang, C.; Kievit, F. M.; Veis, O.; Stephen, Z. R.; Wang, T.; Lee, D.; Ellenbogen, R. G.; Zhang, M. Fabrication of Magnetic Nanoparticles with Controllable Drug Loading and Release through a Simple Assembly Approach. *J. Controlled Release* **2012**, *162*, 233–241.
31. Gautier, J.; Munnier, E.; Paillard, A.; Hervé, K.; Douziech-Eyrolles, L.; Soucé, M.; Dubois, P.; Chourpa, I. A Pharmaceutical Study of Doxorubicin-Loaded PEGylated Nanoparticles for Magnetic Drug Targeting. *Int. J. Pharm.* **2012**, *423*, 16–25.
32. Duong, H. T. T.; Marquis, C. P.; Whittaker, M.; Davis, T. P.; Boyer, C. Acid Degradable and Biocompatible Polymeric Nanoparticles for the Potential Co-delivery of Therapeutic Agents. *Macromolecules* **2011**, *44*, 8008–8019.
33. Sanson, C.; Diou, O.; Thévenot, J.; Ibarboure, E.; Soum, A.; Brûlet, A.; Miraux, S.; Thiaudière, E.; Tan, S.; Brisson, A.; et al. Doxorubicin Loaded Magnetic Polymeric Nanoparticles: Theranostic Nanocarriers for MR Imaging and Magneto-Chemotherapy. *ACS Nano* **2011**, *5*, 1122–1140.
34. Nasongkla, N.; Bey, E.; Ren, J.; Ai, H.; Khemtong, C.; Guthi, J. S.; Chin, S.-F.; Sherry, A. D.; Boothman, D. A.; Gao, J. Multifunctional Polymeric Micelles as Cancer-Targeted, MRI-Ultrasensitive Drug Delivery Systems. *Nano Lett.* **2006**, *6*, 2427–2430.
35. Hu, J.; Qian, Y.; Wang, X.; Liu, T.; Liu, S. Drug-Loaded and Superparamagnetic Iron Oxide Nanoparticle Surface-Embedded Amphiphilic Block Copolymer Micelles for Integrated Chemotherapeutic Drug Delivery and MR Imaging. *Langmuir* **2011**, *28*, 2073–2082.
36. Gaihre, B.; Khil, M. S.; Kim, H. Y. *In Vitro* Anticancer Activity of Doxorubicin-Loaded Gelatin-Coated Magnetic Iron Oxide Nanoparticles. *J. Microencapsulation* **2011**, *28*, 286–293.
37. Munnier, E.; Cohen-Jonathan, S.; Hervé, K.; Linassier, C.; Soucé, M.; Dubois, P.; Chourpa, I. Doxorubicin Delivered to MCF-7 Cancer Cells by Superparamagnetic Iron Oxide Nanoparticles: Effects on Subcellular Distribution and Cytotoxicity. *J. Nanopart. Res.* **2011**, *13*, 959–971.
38. Kaaki, K.; Hervé-Aubert, K.; Chiper, M.; Shkilnyy, A.; Soucé, M.; Benoit, R.; Paillard, A.; Dubois, P.; Saboungi, M.-L.; Chourpa, I. Magnetic Nanocarriers of Doxorubicin Coated with Poly(ethylene glycol) and Folic Acid: Relation between Coating Structure, Surface Properties, Colloidal Stability, and Cancer Cell Targeting. *Langmuir* **2012**, *28*, 1496–1505.
39. Javid, A.; Ahmadian, S.; Saboury, A. A.; Kalantar, S. M.; Rezaei-Zarchi, S. Chitosan Coated Superparamagnetic Iron Oxide Nanoparticles for Doxorubicin Delivery: Synthesis and Anticancer Effect against Human Ovarian Cancer Cells. *Chem. Biol. Drug Des.* **2013**, *82*, 296–306.

40. Deng, L.; Wang, G.; Ren, J.; Zhang, B.; Yan, J.; Li, W.; Khashab, N. M. Enzymatically Triggered Multifunctional Delivery System based on Hyaluronic Acid Micelles. *RSC Adv.* **2012**, *2*, 12909–12914.

41. Zhang, X. F.; Mansouri, S.; Clime, L.; Ly, H. Q.; Yahia, L. H.; Veres, T. Fe<sub>3</sub>O<sub>4</sub>-Silica Core-Shell Nanoporous Particles for High-Capacity pH-Triggered Drug Delivery. *J. Mater. Chem.* **2012**, *22*, 14450–14457.

42. Li, W. M.; Chen, S. Y.; Liu, D. M. *In Situ* Doxorubicin-CaP Shell Formation on Amphiphilic Gelatin-Iron Oxide Core as a Multifunctional Drug Delivery System with Improved Cytocompatibility, pH-Responsive Drug Release and MR Imaging. *Acta Biomater.* **2013**, *9*, 5360–5368.

43. Zhao, Z.; Huang, D.; Yin, Z.; Chi, X.; Wang, X.; Gao, J. Magnetite Nanoparticles as Smart Carriers to Manipulate the Cytotoxicity of Anticancer Drugs: Magnetic Control and pH-Responsive Release. *J. Mater. Chem.* **2012**, *22*, 15717–15725.

44. Liu, J.; Duong, H.; Whittaker, M. R.; Davis, T. P.; Boyer, C. Synthesis of Functional Core, Star Polymers via RAFT Polymerization for Drug Delivery Applications. *Macromol. Rapid Commun.* **2012**, *33*, 760–766.

45. Yang, X.; Grailer, J. J.; Rowland, I. J.; Javadi, A.; Hurley, S. A.; Matson, V. Z.; Steeber, D. A.; Gong, S. Multifunctional Stable and pH-Responsive Polymer Vesicles Formed by Heterofunctional Triblock Copolymer for Targeted Anticancer Drug Delivery and Ultrasensitive MR Imaging. *ACS Nano* **2010**, *4*, 6805–6817.

46. Hurley, K. R.; Lin, Y.-S.; Zhang, J.; Egger, S. M.; Haynes, C. L. Effects of Mesoporous Silica Coating and Postsynthetic Treatment on the Transverse Relaxivity of Iron Oxide Nanoparticles. *Chem. Mater.* **2013**, *25*, 1968–1978.

47. Boyer, C.; Bulmus, V.; Priyanto, P.; Teoh, W. Y.; Amal, R.; Davis, T. P. The Stabilization and Bio-functionalization of Iron Oxide Nanoparticles Using Heterotrihelical Polymers. *J. Mater. Chem.* **2009**, *19*, 111–123.

48. Boyer, C.; Priyanto, P.; Davis, T. P.; Pissuwan, D.; Bulmus, V.; Kavallaris, M.; Teoh, W. Y.; Amal, R.; Carroll, M.; Woodward, R.; et al. Anti-Fouling Magnetic Nanoparticles for siRNA Delivery. *J. Mater. Chem.* **2010**, *20*, 255–265.

49. Gerweck, L. E.; Vijayappa, S.; Kozin, S. Tumor pH Controls the *In Vivo* Efficacy of Weak Acid and Base Chemotherapeutics. *Mol. Cancer Ther.* **2006**, *5*, 1275–1279.

50. Tannock, I. F.; Rotin, D. Acid pH in Tumors and Its Potential for Therapeutic Exploitation. *Cancer Res.* **1989**, *49*, 4373–4384.

51. Chang, Y.-L.; Meng, X.-L.; Zhao, Y.-L.; Li, K.; Zhao, B.; Zhu, M.; Li, Y.-P.; Chen, X.-S.; Wang, J.-Y. Novel Water-Soluble and pH-Responsive Anticancer Drug Nanocarriers: Doxorubicin-PAMAM Dendrimer Conjugates Attached to Superparamagnetic Iron Oxide Nanoparticles (IONPs). *J. Colloid Interface Sci.* **2011**, *363*, 403–409.

52. Fleige, E.; Quadir, M. A.; Haag, R. Stimuli-Responsive Polymeric Nanocarriers for the Controlled Transport of Active Compounds: Concepts and Applications. *Adv. Drug Delivery Rev.* **2012**, *64*, 866–884.

53. Watson, P.; Jones, A. T.; Stephens, D. J. Intracellular Trafficking Pathways and Drug Delivery: Fluorescence Imaging of Living and Fixed Cells. *Adv. Drug Delivery Rev.* **2005**, *57*, 43–61.

54. Carroll, M. R. J.; Huffstetler, P. P.; Miles, W. C.; Goff, J. D.; Davis, R. M.; Riffle, J. S.; House, M. J.; Woodward, R. C.; Pierre, T. G. S. The Effect of Polymer Coatings on Proton Transverse Relaxivities of Aqueous Suspensions of Magnetic Nanoparticles. *Nanotechnology* **2011**, *22*, 325702.

55. Saville, S. L.; Woodward, R. C.; House, M. J.; Tokarev, A.; Hammersqq, J.; Qi, B.; Shaw, J.; Saunders, M.; Varsani, R. R.; St; Pierre, T. G.; et al. The Effect of Magnetically Induced Linear Aggregates on Proton Transverse Relaxation Rates of Aqueous Suspensions of Polymer Coated Magnetic Nanoparticles. *Nanoscale* **2013**, *5*, 2152–2163.

56. Denard, B.; Lee, C.; Ye, J. Doxorubicin Blocks Proliferation of Cancer Cells through Proteolytic Activation of CREB3L1. *eLife* **2012**, *1*, e00090.

57. Dai, X. W.; Yue, Z. L.; Eccleston, M. E.; Swartling, J.; Slater, N. K. H.; Kaminski, C. F. Fluorescence Intensity and Lifetime Imaging of Free and Micellar-Encapsulated Doxorubicin in Living Cells. *Nanomedicine (New York, NY, U. S.)* **2008**, *4*, 49–56.

58. Hovorka, O.; Subr, V.; Vetzicka, D.; Kovar, L.; Strohalm, J.; Strohalm, M.; Benda, A.; Hof, M.; Ulbrich, K.; Rihova, B. Spectral Analysis of Doxorubicin Accumulation and the Indirect Quantification of its DNA Intercalation. *Eur. J. Pharm. Biopharm.* **2010**, *76*, 514–524.

59. Bakker, G.-J.; Andresen, V.; Hoffman, R. M.; Friedl, P. In *Methods in Enzymology*; Conn, P. M., Ed.; Academic Press: Waltham, MA, 2012; Vol. 504, pp 109–125.

60. Duong, H. T. T.; Hughes, F.; Sagnella, S.; Kavallaris, M.; MacMillan, A.; Whan, R.; Hook, J.; Davis, T. P.; Boyer, C. Functionalizing Biodegradable Dextran Scaffolds Using Living Radical Polymerization: New Versatile Nanoparticles for the Delivery of Therapeutic Molecules. *Mol. Pharmaceutics* **2012**, *9*, 3046–3061.

61. Broussard, J. A.; Rappaz, B.; Webb, D. J.; Brown, C. M. Fluorescence Resonance Energy Transfer Microscopy as Demonstrated by Measuring the Activation of the Serine/Threonine Kinase Akt. *Nat. Protoc.* **2013**, *8*, 265–281.

62. Chen, N.-T.; Wu, C.-Y.; Chung, C.-Y.; Hwu, Y.; Cheng, S.-H.; Mou, C.-Y.; Lo, L.-W. Probing the Dynamics of Doxorubicin-DNA Intercalation during the Initial Activation of Apoptosis by Fluorescence Lifetime Imaging Microscopy (FLIM). *PLoS ONE* **2012**, *7*, e44947.

63. Jameson, D. M.; Gratton, E.; Hall, R. D. The Measurement and Analysis of Heterogenous Emissions by Multifrequency Phase and Modulation Fluorometry. *Appl. Spectrosc. Rev.* **1984**, *20*, 55–106.

64. Redford, G. I.; Clegg, R. M. Polar Plot Representation for Frequency-Domain Analysis of Fluorescence Lifetimes. *J. Fluoresc.* **2005**, *15*, 805–815.

65. Digman, M. A.; Caiola, V. R.; Zamai, M.; Gratton, E. The Phasor Approach to Fluorescence Lifetime Imaging Analysis. *Biophys. J.* **2008**, *94*, L14–L16.

66. Kunz-Schughart, L. A.; Freyer, J. P.; Hofstaedter, F.; Ebner, R. The Use of 3-D Cultures for High-Throughput Screening: The Multicellular Spheroid Model. *J. Biomol. Screening* **2004**, *9*, 273–285.

67. Mueller-Klieser, W. Tumor Biology and Experimental Therapeutics. *Crit. Rev. Oncol./Hematol.* **2000**, *36*, 123–139.

68. Hamilton, G. Multicellular Spheroids as an *In Vitro* Tumor Model. *Cancer Lett.* **1998**, *131*, 29–34.

69. Lin, R.-Z.; Chang, H.-Y. Recent Advances in Three-Dimensional Multicellular Spheroid Culture for Biomedical Research. *Biotechnol. J.* **2008**, *3*, 1172–1184.

70. LaBarbera, D. V.; Reid, B. G.; Yoo, B. H. The Multicellular Tumor Spheroid Model for High-Throughput Cancer Drug Discovery. *Expert Opin. Drug Discovery* **2012**, *7*, 819–830.

71. Kimlin, L. C.; Casagrande, G.; Virador, V. M. *In Vitro* Three-Dimensional (3D) Models in Cancer Research: An Update. *Mol. Carcinog.* **2013**, *52*, 167–182.

72. Mehta, G.; Hsiao, A. Y.; Ingram, M.; Luker, G. D.; Takayama, S. Opportunities and Challenges for Use of Tumor Spheroids as Models to Test Drug Delivery and Efficacy. *J. Controlled Release* **2012**, *164*, 192–204.

73. Pampaloni, F.; Reynaud, E. G.; Stelzer, E. H. K. The Third Dimension Bridges the Gap between Cell Culture and Live Tissue. *Nat. Rev. Mol. Cell Biol.* **2007**, *8*, 839–845.

74. Ma, H. L.; Jiang, Q.; Han, S.; Wu, Y.; Cui Tomshine, J.; Wang, D.; Gan, Y.; Zou, G.; Liang, X. J. Multicellular Tumor Spheroids as an *In Vivo* Like Tumor Model for Three-Dimensional Imaging of Chemotherapeutic and Nano Material Cellular Penetration. *Mol. Imaging* **2012**, *11*, 487–498.

75. Denk, W.; Strickler, J. H.; Webb, W. W. Two-Photon Laser Scanning Fluorescence Microscopy. *Science* **1990**, *248*, 73–76.

76. AbD Serotec, *amarBlue Worked Example 1 - Cell Line a549*, <http://www.abdserotec.com/amarblue-example-1.html>.

77. Friedrich, J.; Seidel, C.; Ebner, R.; Kunz-Schughart, L. A. Spheroid-Based Drug Screen: Considerations and Practical Approach. *Nat. Protoc.* **2009**, *4*, 309–324.